Research article

Comparative simulation of nonlinear radiative nano casson and maxwell fluids with periodic magnetic force and sensitivity analysis

Saiful Islam [a], Md Yousuf Ali [b], Sk Reza-E-Rabbi [c,*]

[a] Department of Mathematics, Bangabandhu Sheikh Mujibur Rahman Science and Technology University, Gopalganj, 8100, Bangladesh
[b] Department of Computer Science and Engineering, Daffodil International University, Dhaka, 1216, Bangladesh
[c] Mathematics Discipline, Khulna University, Khulna, 9208, Bangladesh

ARTICLE INFO

ABSTRACT

This study investigated cyclic magneto-hydrodynamic radiative effects in Casson and Maxwell fluids, including nonlinear radiation and Arrhenius activation energy. It promotes non-Newtonian fluid use in diverse fields like industry, manufacturing, sciences, medicine, and engineering. Using boundary layer approximations, non-dimensional equations are formulated. For numerical solutions, widely recognized explicit finite difference method (EFDM) has been utilized. To ensure the robustness of EFDM results, stability and convergence tests are performed. Exploration involve a detailed sensitivity analysis by using RSM, offering a thorough understanding of influential parameters. These analyses explore complex interactions among physical parameters, affecting Nusselt number, skin friction, and Sherwood number. Maxwell fluid's velocity is more affected by periodic magnetic force than Casson fluid, during the presence of nonlinear radiation. Additionally, nonlinear thermal radiation has a greater impact on temperature and concentration profiles compared to linear radiation for both fluids. Moreover, Casson fluid has a stronger influence on the average heat transfer rate compared to Maxwell fluid with nonlinear thermal radiation which is 8.6 % greater than the Maxwell fluid. On the other hand, at constant thermal radiation (Ra), due to decrease of Brownian motion (Nb), the rate of heat transfer is reduced by 1.2 % and 0.3 % respectively for Maxwell and Casson fluid. Also, for thermophoresis parameter (Nt), this rate is reduced by 2 % and 1.6 % respectively. The investigation also revealed that the Ra exhibits a positive sensitivity towards average Nusselt number, while Nb and Nt are displayed a negative sensitivity.

1. Introduction

Nowadays, modern nanotechnology gives innovative scopes to produce and process different sorts of manufacturing materials with traditional crystallite sizes less than 100 nm. For this reason, research on nanofluid is becoming much better interesting from the last few years. In 1995 from Argonne National Laboratory in the U.S.A, Choi et al. [1] introduced a fluid mixture that contained solid nanoparticles (for example: Cu, CuO, Ag, Al_2O_3, TiO_2 etc.) which was called nanofluid. In fact, these solid particles are stably and uniformly distributed into a base fluid (such as: water, engine oil, pump oil, ethylene glycol, etc.). It is anticipated that nanofluid will

be the foreseeable future of heat transfer fluids since it offers novel opportunities to enhance heat transfer execution with regard to pure liquids. Moreover, due to the unique superior thermal performance, chemical properties, and physical properties of nanofluid, it plays a significant role in abundant industrial and technological applications. Furthermore, nanofluid can grow abrasion-related properties rather than fluid mixtures/conventional solid. Typically, these dispersed nanoparticles increase the thermal conductivity of nanofluids (normally metal or metal oxide). This unique property of nanofluid has a lot of uses in thermal process which include hybrid-powered engines, heat exchanger, fuel cells, pharmaceutical processes, nuclear reactors, industrial freezing, smart fluids, microelectronics, nanofluids coolant, and withdrawal of geothermal power. In recent years, a number of investigations on nanofluids have been completed by various researchers. Beg et al. [2] analyzed mixed convective nanomaterial flow through porous space originating from exponential stretched sheet. Biswas et al. [3] studied a dense gray nanofluid model through a vertical plate. Furthermore, to complete their work, an explicit finite difference method was used where temperature, concentration, and velocity profile were investigated graphically. Between two heated rotating disks Hayat et al. [4] investigated entropy for a radiative water based nanofluid. With the presence of two different nanoparticles into base fluid, Wang et al. [5] presented a numerical analysis on a microchannel porous media. On the other hand, over a stretched nonlinear surface, Mamun et al. [6] investigated Sisko-nanofluid flow by considering thermal radiation and magnetohydrodynamic (MHD) effect. Actually, MHD refers to the research that examines the effects of magnetism in electrically conducting fluids. Very recently, Xu et al. [7] described the mode of heat transfer of metal foam and nanofluid in a porous medium. Again, Asadi et al. [8] considered thermal properties, heat transfer efficiency, colloidal dispersion, and numerous ultra-sonication parameters for different nanofluids models where they concluded that uninterrupted ultra-sonication breaks down the outsized clusters into the minor clusters of nanoparticles. Kamel et al. [9] expressed boiling heat transfer properties for nanofluids with convective heat transfer and pool flow boiling for a nanofluid. Furthermore, recently, several investigations were completed on the nanofluid flow with the purpose of regulating the heat transfer mechanisms in various systems [10,11]. Also, Esfe et al. [12] expolred the natural convective heat transfer behaviour on a U-shaped cavity. Hayat et al. [13] studied on entropy generation for the radiative flow of nanomaterials across two heated spinning disks. Sayed et al. [14] employed Legendre-Galerkin method to examine the nanofluid flow across an upward cone and how heat transfers under the impacts of thermal radiation and heat creation.

Researchers' interest in non-Newtonian fluids has increased in the modern era due to growing its uses in the fields of industrial processes and manufacturing, applied science, medical and engineering. In fact, a fluid whose flow curve is not linear, which doesn't convey the Newtonian law of viscosity, is entitled as a non-Newtonian fluid. Once more, the deceptive viscosity of a non-Newtonian fluid varies for a wide range of values of temperature and pressure. The most liquids, such as tomato ketchup, condensed milk, apple sauce, sugar solution, soap mud, shampoo, suspension solutions, animal blood, and exotic lubricants show the properties of non-Newtonian fluids which have taken an imperative place by this time in human life. Due to the fact that a specific fluid model did not calculate all of the non-Newtonian fluids' physical characteristics so in different times a lot of scholars recommended various non-Newtonian fluids models [15,16]. Such as, a power-law non-Newtonian fluid in deformable, fractured porous media was investigated by Hageman et al. [17]. Mustafa et al. [18] quantitatively evaluated the effects of a helical absorber tube on the thermal efficiency of a solar collector (PTSC) filled with non-Newtonian nanofluid. Ali et al. [19] used the finite element technique to study heat and mass transmission in Jeffrey and Oldroyd-B nanofluids in the existence of chemical processes and radiation. Raihan et al. [20] conducted research on non-Newtonian fluids with unique rheological characteristics and water using a planar single-cavity micro channel. Actually, three main categories of these fluid models-integral, rate, and differential-were used to categorize them. The rate type and differential type have drawn the most attention of these three categories but specifically, the subclass of rate type model of non-Newtonian fluids is used widely which is known as Maxwell fluid, introduced by Maxwell in 1867 [21]. Moreover, Maxwell fluid demonstrates both elasticity and viscosity properties. This fluid model does not accurately talk about the usual correlation between shear stress and shear rate for a simple shear flow, nevertheless, this fluids model has acquired a number of successes to refer to the features of optical fibers, numerous polymeric liquids of small molecular weight, and many others. Furthermore, this fluid model can be anticipated the effects of relaxation time which cannot possible to calculate by any other differential-type fluids. In different times, diverse efforts have been taken by considering Maxwell fluid model such as: to explain heat transfer for steady Maxwell fluid, Abel et al. [22] made numerical computations through a stretching sheet. Again, in another study, for a mixed convection Maxwell fluid the Cattaneo-Christov model by inconstant thickness sheet was studied by Hayat et al. [23]. With the manifestation of nanoparticles, Arifuzzaman et al. [24] scrutinized MHD flow Maxwell fluid vertical porous plate where the effects of chemical reactions, radiation absorption, and heat generation were considered. Ahmad et al. [25] looked at the flow of a 3D Maxwell nanofluid with variable viscosity and thermal conductivity across a stretched surface. Safdar et al. [26] used gyrotactic microorganisms across a porous stretched sheet to theoretically and numerically study MHD Maxwell nanofluid flow.

Due of its significance in several domains such as polymer extrusion, pharmaceutical process, purification of crude oil, paints, petroleum industry, fluid droplet sprays, glass fiber drawing, and several others, the Casson fluid (honey, soup, tomato sauce, human blood, concentrated fruit juices, jelly, etc.), another non-Newtonian fluid, has recently drawn the attention of current researchers. This fluid, which was expressed by Casson in 1959 [27], has distinct features. This fluid demonstrates rheological characteristics. Compared to Newtonian fluid, this fluid exhibits stress-strain relationships that are significantly different. It behaves as a solid body when the shear stress is less than the yield stress. On the other side, it starts to move when shear stress exceeds yield stress. The Casson fluid has recently experienced greater success in numerical and experimental studies, making it a more popular research topic than any other non-Newtonian fluid models. For these useful applications, numerous researchers have analyzed the Casson fluid flow through dissimilar geometries with adding different effects [28,29]. Chen et al. [30] studied a 2D heat transfer phenomena of a non-conducting Casson fluid across a surface that stretched using thermophoretic particle deposition. A magnetic dipole was used to interact with an external magnetic field. Bilal et al. [31] discussed the consequences of a radiative Casson fluid over a Riga surface which was

chemically reactive, and concluded that increasing the chemical reaction and heat absorption parameters caused a decrease in momentum distributions. Khan et al. [32] investigated an unsteady radiating stagnation point flow of a Casson fluid through a porous shrinking/stretching surface using an external magnetic field, and a non-uniform heat source, and solved the related ODEs using MATLAB's bvp4c built-in function. In a stenotic tube with an absorptive wall, Das et al. [33] accompanied a study on blood using the Casson model. Over a stretching sheet, the H_2O–Fe_3O_4-MWCNT hybrid nanofluid flow, which includes dust particles, was scrutinized by Khan et al. [34] to see how Lorentz forces affected the flow. Dawar et al. [35] studied the flow of a Casson fluid containing gyrotactic microorganisms in both magnetized and non-magnetized conditions over a stratified stretched cylinder. Sulochana et al. [36] expressed a 3D Casson nanofluid model on a stretched sheet to analyze the rheological characteristics, and the Runge-Kutta (RK) process was used to get velocity, temperature, and concentration profiles. With the existence of the effects of thermal radiation, Lorentz force, heated horizontal wall, and motion of nanoparticles, Thumma et al. [37] described a time dependent 3D Casson fluid by the generalized differential quadrature method. Again, through a horizontal circular duct, the hydro-magnetic effects of blood flow were described by Ali et al. [38]. With the presence of magnetic nanoparticles on a stenosis artery, Priyadharshini et al. [39] inspected the effect of MHD for blood flow. To inspect the flow behavior of a steady Casson fluid, that is electrically conducted, Ali et al. [40] expressed another model by using Darcy's law in a 2D constricted walls channel through a porous medium. Bukhari et al. [41] recently conducted another analysis for a pulsatile Casson fluid flow in a rectangular channel with the appearance of heat radiation and magnetic field. Awais et al. [42] looked at the consequences of heat generation, the Lorentz force, and the mass as well as heat transfer of an MHD Casson fluid flow over a diminishing porous wall. Furthermore, many scientific and technical fields such as processing of food, nuclear reactor's cooling, oil emulsions, geothermal reservoirs, and chemical engineering contain mass transfer occurrence carried out by chemical reaction and activation energy which has been given spectacular consideration due to these distinct useful applications. When there exists a concentration difference of different species in a mixture then the mass transfer arises for this mixture. The concentration of these species changes simultaneously from upper to lesser concentration. The amount of least energy required for performing a definite chemical reaction is known as activation energy. Generally, the Arrhenius equation for activation energy is expressed by the form [43]; $K = B\left(\frac{T}{T_\infty}\right)^n \exp\left(\frac{-E_a}{\kappa T}\right)$, where $K, B, T, T_\infty, n, E_a, \kappa$ denotes the reaction rate constant, pre-exceptional factor, ambient temperature, fixed-rate constant, activation energy, and Boltzmann constant respectively. The chemical process and Arrhenius activation energy were first introduced by Bestman et al. [44] in 1991, and explained how a porous media and heat and mass transfer work together. Subsequently, to analyze the consequence of activation energy for heat and mass transfer Khan et al. [45] developed another unsteady free convective flow model. For a second-grade nanofluid flow, Kalaivanan et al. [46] figure out the effect of activation energy and concluded that the concentration profile expands by means of activation energy. For bi-convective Casson nanofluid model the Darcy-Forchheimer was investigated by Saeed et al. [47] by considering Arrhenius activation energy over a rotating disk. Subsequently, Shi et al. [48] analyzed the consequence of activation energy for bioconvective Cross-nanofluid over a stretching surface. The previous study by Ahmed et al. [49] examined linear and nonlinear radiation patterns in the setting of MHD non-Newtonian nanofluid flow with Arrhenius activation energy. In the end, their research revealed that the activation energy has a significant impact on how the Maxwell fluid and nonlinear radiation interact, which has implications for both industrial use and cancer therapy. Ali et al. [50] conducted a thorough investigation of hydro-magnetic flow including Casson fluid over a stretched sheet, focusing on the combined effects of thermoelectric and thermal radiation processes. Their results highlighted a stronger influence on non-Newtonian (Casson) fluid than on its Newtonian equivalent. Mass and heat movement were numerically analyzed by Dharmaiah et al. [51], accounting for temperature conditions and activation energy. Their investigation showed that the impact of activation energy is what causes the concentration to increase. Furthermore, the authors [52] examined the effect of nonlinear thermal radiation on Jeffrey fluid flow and found that the Nusselt number increases as the radiation parameter increases. Furthermore, as the Casson parameter increased, the researchers [53] saw a rise in the temperature of blood flow. The investigation by Kumar et al. [54] concentrated on the transitory circumstances influencing Casson fluid flow when magnetic influences are present. Their results showed that the influence of Casson parameters led to improvements in temperature and concentration. A research on MHD flow in the presence of heat radiation and activation energy was carried out by Shankar Goud et al. [55]. As the melting parameters increased, they observed a decrease in velocity that was mirrored on the momentum boundary layer.

The goal of this study is to investigate the pace at which the periodic magnetic parameters and Arrhenius activation energy interact with nonlinear radiative Maxwell and Casson nanofluid flow on a stretching surface. To the author's best knowledge, prior to this study, there had been no dedicated research in the literature that investigated periodic magneto-hydrodynamics of Casson and Maxwell fluids, considering both nonlinear radiation effects and Arrhenius activation energy in the context of flow over an enlarging surface. Furthermore, the response surface methodology (RSM) is involved to analysis the sensitivity rate of the involved significant factors for both Casson and Maxwell fluids. This study is a significant attempt to fill this substantial gap in scholarly exploration. The following is a list of the specific goals of this numerical investigation.

- To investigate periodic magnetic force, nonlinear thermal radiation, mass diffusion, and radiation absorption effects on unsteady chemically reactive Casson and Maxwell fluid flow with nanoparticles across a stretching surface.
- To simulate the governing equations using the recognized explicit finite difference technique (EFDM).
- To analyze the stability and convergence test of EFDM solutions for choosing suitable values for the involved parameters.
- To explore 2D and 3D response surfaces, and sensitivity analysis of comprehending key variables using graphical representations.
- To examine how different physical parameters with other effects affect various important flow fields.
- To depict streamlines and isotherms in order to demonstrate proficient fluid flow visualization.

Finally, the physical characteristics of the various parameters have been researched here, and this study has also been validated. A general framework of this numerical investigation is represented in Fig. 1.

2. Problem formulation

The enactment of 2D unsteady radiative periodic magnetic hydrodynamics Casson and Maxwell fluids with nonlinear thermal radiation, actuality of nanoparticles, and Arrhenius activation energy are analyzed in this article. Due to stretching constant B, here the fluid velocity is assumed to be $u = Bx$, and an external magnetic field B_0 is acted along Y-axis. The X-axis represented the direction of stretching, while the Y-axis was taken perpendicular to the surface. Also, T stands for the temperature of the fluid, and C for the concentration next to the wall which is get raised at t > 0. Additionally, U_∞, T_∞ and C_∞ denote the fluid's velocity, temperature, and concentration far from the wall, respectively that is described in Fig. 2.

The rheological expression for an incompressible Casson fluid model is defined in equation (1) as:

$$\tau_{ij} = \begin{cases} \left(2\mu_b + \sqrt{\dfrac{2}{\pi}} E_y\right) e_{ij} \text{ if } \pi > \pi_c \\[4mm] \left(2\mu_b + \sqrt{\dfrac{2}{\pi_c}} E_y\right) e_{ij} \text{ if } \pi < \pi_c \end{cases} \tag{1}$$

where μ_b is the non-Newtonian fluid's plastic dynamic viscosity, the crucial component of this product is π_c, the element deformation rate in relation to itself is π, fluid's yield stress is represented by E_y, and the $(i, j)^{\text{th}}$ component of the deformation rate is shown by the symbol e_{ij}. Therefore, it behaves like a fluid when share stress is greater than yield stress. Conversely, it behaves as a solid body when share stress is lower than yield stress. Again, $E_y = \frac{\mu_b}{\beta}\sqrt{2\pi}$. That is, $\upsilon' = \upsilon\left(1 + \frac{1}{\beta}\right)$ where ρ and υ stand for density and kinematic viscosity of the base fluid, and β represents the non-Newtonian Casson factor.

2.1. Continuity equation

The continuity equation is another name for the conservation law of mass, and the continuity equation for incompressible laminar flow (in vector form) is: $\Delta.q = 0$, where $q = u\widehat{i} + v\widehat{j}$ indicates velocity vector and Δ is the vector differential operator. In Cartesian coordinate system, this continuity equation is expressed by:

$$\frac{\partial u}{\partial x} + \frac{\partial u}{\partial y} = 0 \tag{2}$$

2.2. Momentum equation

In fluid dynamics, we employ the momentum equation, based on Newton's second law of motion. Specifically, for incompressible fluid flow, equation (3) is often referred to as the Navier-Stokes equation, and its vector form is:

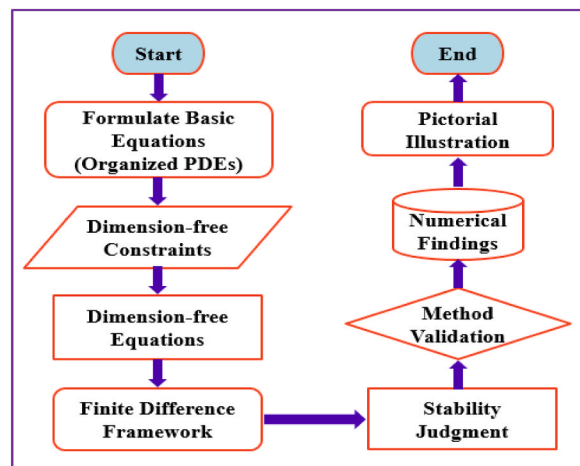$$\frac{\partial q}{\partial t} = -\frac{1}{\rho}\nabla p + \upsilon\nabla^2 q - (\nabla.q)q + F \tag{3}$$

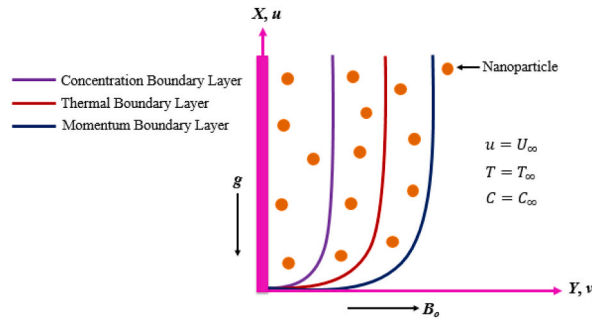**Fig. 1.** General procedure to complete this work.

Fig. 2. Physical configuration of this fluid flow.

where v, ρ, p, F are the kinematic viscosity, density, pressure, and body force of fluid. The external forces as like buoyancy force, magnetic effect are considered as body force for this fluid model. Moreover, for Casson fluid, the viscous factor v will be replaced by $\left(1 + \frac{1}{\beta}\right)v$. Also, for Maxwell fluid, another effect $-\lambda\left(u^2\frac{\partial^2 u}{\partial x^2} + v^2\frac{\partial^2 u}{\partial y^2} + 2uv\frac{\partial^2 u}{\partial x \partial y}\right)$ will be included with body forces. So, the above vector expression of momentum equation for both Casson and Maxwell fluid can be represented in Cartesian coordinate as like [24,28]:

$$\frac{\partial u}{\partial t} + u\frac{\partial u}{\partial x} + v\frac{\partial u}{\partial y} = -\lambda\left(u^2\frac{\partial^2 u}{\partial x^2} + v^2\frac{\partial^2 u}{\partial y^2} + 2uv\frac{\partial^2 u}{\partial x \partial y}\right)v\left(1 + \frac{1}{\beta}\right)\left(\frac{\partial^2 u}{\partial y^2}\right) - \frac{\sigma B_0^2}{\rho}\sin^2\left(\frac{\pi x}{\lambda}\right)u + g\beta_T(T - T_\infty) + g\beta_C(C - C_\infty) - \left(1 + \frac{1}{\beta}\right)\frac{vu}{k_1}$$

(4)

2.3. Energy equation

For fluid flow, the energy equation expresses the conservation law of energy i.e., energy balance of a system. For incompressible fluid, the vector form of energy equation is:

$$\frac{\partial T}{\partial t} + q.\nabla T = \frac{1}{\rho c_p}\left[\nabla.(\kappa \nabla T) + \rho c_p\frac{D_T}{T_\infty}D_B(\nabla T.\nabla T) + \rho c_p D_B(\nabla T.\nabla C)\right]$$

(5)

In Cartesian coordinate system, the above equation (5) for Casson and Maxwell fluid is represented in the following form considering boundary layer approximation and heat radiation [56]:

$$\frac{\partial T}{\partial t} + u\frac{\partial T}{\partial x} + v\frac{\partial T}{\partial y} = \frac{\kappa}{\rho c_p}\left(\frac{\partial^2 T}{\partial y^2}\right) + \tau\left[D_B\left(\frac{\partial T}{\partial y}\frac{\partial C}{\partial y}\right) + \frac{D_T}{T_\infty}\left(\frac{\partial T}{\partial y}\right)^2\right] + \left(1 + \frac{1}{\beta}\right)\frac{v}{c_p}\left(\frac{\partial u}{\partial y}\right)^2 - \frac{\sigma B_0^2}{\rho c_p}\sin^2\left(\frac{\pi x}{\lambda}\right)u^2 - \frac{1}{\rho c_p}\frac{\partial q_r}{\partial y}$$

Here, $q_r = \frac{-16\sigma^* T^3}{3k^*}\frac{\partial T}{\partial y}$. In this context, σ^* and k^* denote the constants commonly referred to as the Stefan-Boltzmann constant and the mean absorption coefficient, respectively. Hence, the above equation becomes:

$$\frac{\partial T}{\partial t} + u\frac{\partial T}{\partial x} + v\frac{\partial T}{\partial y} = \frac{\kappa}{\rho c_p}\left(\frac{\partial^2 T}{\partial y^2}\right) + \tau\left[D_B\left(\frac{\partial T}{\partial y}\frac{\partial C}{\partial y}\right) + \frac{D_T}{T_\infty}\left(\frac{\partial T}{\partial y}\right)^2\right] + \left(1 + \frac{1}{\beta}\right)\frac{v}{c_p}\left(\frac{\partial u}{\partial y}\right)^2 - \frac{\sigma B_0^2}{\rho c_p}\sin^2\left(\frac{\pi x}{\lambda}\right)u^2 - \frac{1}{\rho c_p}\frac{16\sigma}{3k^*}\left[T^2\left(\frac{\partial T}{\partial y}\right)^2 + T^3\frac{\partial^2 T}{\partial y^2}\right]$$

(6)

2.4. Concentration equation

For chemical reaction among a fluid, the vector form of concentration equation of incompressible fluid is:

$$\frac{\partial C}{\partial t} + q.\nabla C = \frac{D_T}{T_\infty}\left(\nabla^2 T\right) + D_B\left(\nabla^2 C\right)$$

(7)

Furthermore, for the boundary layer approximation and the Arrhenius activation energy, the above equation (7) can be represented by in Cartesian form as like [28]:

$$\frac{\partial C}{\partial t} + u\frac{\partial C}{\partial x} + v\frac{\partial C}{\partial y} = D_B\frac{\partial^2 C}{\partial y^2} + \frac{D_T}{T_\infty}\left(\frac{\partial^2 T}{\partial y^2}\right) - Kr^2(C - C_\infty)\left(\frac{T}{T_\infty}\right)^n\exp\left(\frac{-Ea}{\kappa T}\right)$$

(8)

Here, $K = Kr^2(C - C_\infty)\left(\frac{T}{T_\infty}\right)^n\exp\left(\frac{-Ea}{\kappa T}\right)$ denotes the modified Arrhenius equation, Ea represents the activation energy, Kr stands for the reaction rate, n be the fixed rate constants, and Boltzmann constant $\kappa = 8.61 \times 10^{-5}$ eV/K. Also, Brownian diffusivity and the thermophoresis diffusion are D_B and D_T respectively.

Boundary conditions in physics have significant physical implications as they directly affect the behavior and characteristics of the system being studied. Boundary conditions have profound physical implications as they govern the behavior, conservation principles, wave propagation, stability, and response of physical systems to external influences. Properly defining and understanding boundary conditions are essential for accurately modeling and predicting the behavior of systems in various scientific and engineering disciplines. The equivalent initial and boundary conditions are represented in equation (9) as [28]:

$$\text{When } t = 0; \ \{ u = Bx, v = 0, T = T_\infty, C = C_\infty \ \text{ at everywhere} \}$$
$$\text{When } t \geq 0; \ \begin{cases} u = 0, v = 0, T = T_\infty, C = C_\infty & \text{at } x = 0 \\ u = Bx, v = 0, T = T_w, C = C_w & \text{at } y = 0 \\ u = 0, v = 0, T \rightarrow T_\infty, C \rightarrow C_\infty & \text{at } y \rightarrow \infty \end{cases} \tag{9}$$

The velocity in the x direction is equal to Bx at initial time, or when time equals zero, where B denotes the surface's stretching rate. In addition, the temperature and concentration are T_∞ and C_∞, respectively, and the velocity in the y direction is equal to zero. The concentration and temperature remain the same as they were at the beginning of time, but the velocity values in both directions equal zero at the $x = 0$ point when time is higher than zero. Conversely, at $y = 0$ regions, concentration and temperature are T_w (wall temperature) and C_w (wall temperature), respectively, and velocity is equal to Bx in the x direction and $v = 0$. However, when y approaches to infinity, the temperature and concentration both tend to ambient temperature and the values of the velocity in both directions tend to zero. The u and v velocity components, together with the x and y axes, are presented in this situation. Also, to make dimensionless of involved governing equations, we have considered the following variables.

$$u = \frac{v}{\lambda} Gr^{\frac{1}{2}} U, v = \frac{v}{\lambda} Gr^{\frac{1}{4}} V, X = \frac{x}{\lambda}, Y = Gr^{\frac{1}{4}} \frac{y}{\lambda},$$
$$\tau = \frac{v}{\lambda^2} Gr^{\frac{1}{2}} t, \theta = \frac{T - T_\infty}{T_w - T_\infty}, \varphi = \frac{C - C_\infty}{C_w - C_\infty} \tag{10}$$

By using equation (10), equations ((2), (4), (6) and (8)) are obtained as follows:

$$\frac{\partial U}{\partial X} + \frac{\partial V}{\partial Y} = 0 \tag{11}$$

$$\frac{\partial U}{\partial \tau} + U \frac{\partial U}{\partial X} + V \frac{\partial U}{\partial Y} = \left(1 + \frac{1}{\beta} \right) \frac{\partial^2 U}{\partial Y^2} - Nv \left[U^2 \frac{\partial^2 U}{\partial X^2} + 2UV \frac{\partial^2 U}{\partial X \partial Y} + V^2 \frac{\partial^2 U}{\partial Y^2} \right]$$
$$- M^2 \sin^2(\pi X) U + \theta + \left(\frac{Gm}{Gr} \right) \varphi - \left(1 + \frac{1}{\beta} \right) KpU \tag{12}$$

$$\frac{\partial \theta}{\partial \tau} + U \frac{\partial \theta}{\partial X} + V \frac{\partial \theta}{\partial Y} = \frac{1}{Pr} \left[1 + Ra\{ 1 + (\theta_w - 1)\theta \}^3 \right] \frac{\partial^2 \theta}{\partial Y^2} + \left(1 + \frac{1}{\beta} \right) Ec \left(\frac{\partial U}{\partial Y} \right)^2 + Nb \left(\frac{\partial \theta}{\partial Y} \frac{\partial \varphi}{\partial Y} \right) + Nt \left(\frac{\partial \theta}{\partial Y} \right)^2 + EcM^2 U^2 \sin^2(\pi X)$$
$$+ \frac{Ra}{Pr} \{ 1 + (\theta_w - 1)\theta \}^3 \left(\frac{\partial \theta}{\partial Y} \right)^2 \tag{13}$$

$$\frac{\partial \varphi}{\partial \tau} + U \frac{\partial \varphi}{\partial X} + V \frac{\partial \varphi}{\partial Y} = \frac{1}{Le} \frac{\partial^2 \varphi}{\partial Y^2} + \left(\frac{Nt}{Le \, Nb} \right) \frac{\partial^2 \theta}{\partial Y^2} - Kc \ \varphi (1 + \delta\theta)^n \exp \left(\frac{-AE}{1 + \delta\theta} \right) \tag{14}$$

where $Nv = \frac{v\lambda_1}{\lambda^2} Gr^{\frac{1}{2}}$ is Maxwell Parameter, $M^2 = \frac{\sigma\beta_0^2\lambda^2}{\rho v Gr^{\frac{1}{2}}}$ is magnetic parameter, $Gm = \frac{g\beta_C\lambda^3}{v^2}(C_w - C_\infty)$ is mass Grashof number, $Gr = \frac{g\beta_T\lambda^3}{v^2}(T_w - T_\infty)$ is thermal Grashof number, $Kp = \frac{\lambda^2}{k_1 Gr^{\frac{1}{2}}}$ is porous term, $Pr = \frac{v\rho c_p}{\kappa}$ is Prandtl number, $Ra = \frac{16\sigma^* T_\infty^3}{3kk^*}$ is radiation parameter, $\theta_w = \frac{T_w}{T_\infty}$ is the temperature ratio of fluid's, $Ec = \frac{v^2 Gr}{\lambda^2 c_p(T_w - T_\infty)}$ is Eckert number, $Nb = \frac{\tau D_B(C_w - C_\infty)}{v}$ is Brownian motion parameter, $Nt = \frac{\tau D_T(T_w - T_\infty)}{v T_\infty}$ is thermophoresis parameter, $Le = \frac{\alpha}{D_B}$ is Lewis number, $Kc = \frac{\lambda^2 Kr^2}{v Gr^{\frac{1}{2}}}$ is chemical reaction parameter, $\delta = \frac{(T_w - T_0)}{T_\infty}$ is temperature difference factor, $AE = \frac{Ea}{\kappa T_\infty}$ is Arrhenius activation energy parameter.

The local skin friction, Nusselt number, and Sherwood number are illustrated in equation (15) as [58]:

$$Cf = -2.8284 \left(1 + \varepsilon^{-1} \right) Gr^{-\frac{3}{4}} \left(\frac{\partial U}{\partial Y} \right)_{Y=0}, Nu = 0.7071 Gr^{-\frac{3}{4}} \left(\frac{\partial \theta}{\partial Y} \right)_{Y=0} \text{ and } Sh = 0.7071 Gr^{-\frac{3}{4}} \left(\frac{\partial C}{\partial Y} \right)_{Y=0} \tag{15}$$

Moreover, the stream function ψ that is correlated to the velocity constituents as like $U = \frac{\partial \psi}{\partial Y}$ and $V = -\frac{\partial \psi}{\partial U}$, that satisfies the continuity equation (11).

In addition, the corresponding boundary conditions for the non-dimension case are presented in equation (16):

when $\tau \leq 0$; $\{U = 0, V = 0, \theta = 0, C = 0 \quad$ at everywhere

when $\tau > 0$;
$$\begin{cases} U = 0, V = 0, \theta = 0, C = 0 & \text{at } X = 0 \\ U = \beta X = \beta, V = 0, \theta = 1, C = 1 & \text{at } Y = 0 \\ U = 0, V = 0, \theta = 0, C = 0 & \text{as } Y \to \infty \end{cases}$$

(16)

3. Numerical computation

This section outlines the approach for solving the dimensionless governing equations 11–14 along with boundary conditions. Due to the substantial nonlinearity and time-dependent nature of these partial differential equations (PDEs) connected to the boundary conditions, analytical solutions are not feasible. Therefore, we employed a renowned numerical solver known as the finite difference method, originally introduced by Carnahan et al. [57], to obtain a solution for this evolving model. The non-dimensional temperature, velocity, and concentration numerical results in the boundary layer for different non-dimensional parameter values have been computed with EFDM through the FORTRAN program. Once more, the inner boundary layer is separated into grid spaces of lines parallel to the X and Y-axes in order to convince this solver's procedure correctly. As indicated in Fig. 3, the stretching sheet is the X-axis, and the Y-axis is measured perpendicular to the sheet. In the present work, the numerical numbers $X (=20)$ and $Y (=40)$ denote the height of the plate. In addition, $m (=100)$ and $n (=200)$ denote the grid space.

Using explicit finite difference approximation method, equations 11–14 and equation (16) have been converted into equations 17–21

$$\frac{U_{i,j} - U_{i-1,j}}{\Delta X} = -\frac{V_{i,j} - V_{i,j-1}}{\Delta Y}$$

(17)

$$\frac{U'_{i,j} - U_{i,j}}{\Delta \tau} = -U_{i,j}\left(\frac{U_{i,j} - U_{i-1,j}}{\Delta X}\right) - V_{i,j}\left(\frac{V_{i,j+1} - V_{i,j}}{\Delta Y}\right) + \left(1 + \frac{1}{\beta}\right)\left(\frac{U_{i,j+1} - 2U_{i,j} + U_{i,j-1}}{(\Delta Y)^2}\right) - Nv\left[U_{i,j}^2\left(\frac{U_{i+1,j} - 2U_{i,j} + U_{i-1,j}}{(\Delta X)^2}\right)\right]$$

$$- Nv\left[2U_{i,j}V_{i,j}\left(\frac{U_{i+1,j+1} - U_{i+1,j-1} - U_{i-1,j+1} + U_{i-1,j-1}}{4\Delta X \Delta Y}\right)\right] - Nv\left[V_{i,j}^2\left(\frac{U_{i,j+1} - 2U_{i,j} + U_{i,j-1}}{(\Delta Y)^2}\right)\right] - M^2 \sin^2(\pi X(i))U_{i,j} + \theta_{i,j} + \left(\frac{Gm}{Gr}\right)\varphi_{i,j}$$
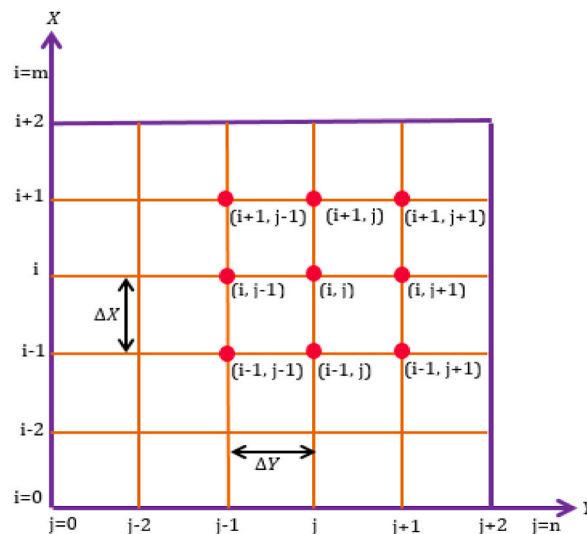
$$- \left(1 + \frac{1}{\beta}\right)KpU_{i,j}\Big\}$$

(18)

Fig. 3. Finite difference grid spacing [58–60].

$$\frac{\theta'_{i,j} - \theta_{i,j}}{\Delta\tau} = -U_{i,j}\left(\frac{\theta_{i,j} - \theta_{i-1,j}}{\Delta X}\right) - V_{i,j}\left(\frac{\theta_{i,j+1} - \theta_{i,j}}{\Delta Y}\right) + \left(1 + \frac{1}{\beta}\right)Ec\left(\frac{U_{i,j+1} - U_{i,j}}{\Delta Y}\right)^2$$

$$+\frac{1}{Pr}\left[1 + Ra\{1 + (\theta_w - 1)\theta_{i,j}\}^3\right]\left(\frac{\theta_{i,j+1} - 2\theta_{i,j} + \theta_{i,j-1}}{(\Delta Y)^2}\right) + EcM^2U_{i,j}^2\sin^2(\pi X(i))$$

$$+Nb\left(\frac{\theta_{i,j+1} - \theta_{i,j}}{\Delta Y}\right)\left(\frac{\varphi_{i,j+1} - \varphi_{i,j}}{\Delta Y}\right) + Nt\left(\frac{\theta_{i,j+1} - \theta_{i,j}}{\Delta Y}\right)^2 + \frac{Ra}{Pr}\{1 + (\theta_w - 1)\theta_{i,j}\}^3\left(\frac{\theta_{i,j+1} - \theta_{i,j}}{\Delta Y}\right)^2\}$$

(19)

$$\frac{\varphi'_{i,j} - \varphi_{i,j}}{\Delta\tau} = \frac{1}{Le}\left(\frac{\varphi_{i,j+1} - 2\varphi_{i,j} + \varphi_{i,j-1}}{(\Delta Y)^2}\right) - U_{i,j}\left(\frac{\varphi_{i,j} - \varphi_{i-1,j}}{\Delta X}\right) - V_{i,j}\left(\frac{\varphi_{i,j+1} - \varphi_{i,j}}{\Delta Y}\right)$$

$$+\left(\frac{Nt}{LeNb}\right)\left(\frac{\theta_{i,j+1} - 2\theta_{i,j} + \theta_{i,j-1}}{(\Delta Y)^2}\right) - Kc\,\varphi_{i,j}\left(1 + \delta\theta_{i,j}\right)^n e^{\left(\frac{-AE}{1 + \delta\theta_{i,j}}\right)}\}$$

(20)

With
$$\left.\begin{array}{l} U_{i,o}^p = 1, T_{i,o}^p = 1, C_{i,o}^p = 1 \\ U_{i,o}^p = 0, T_{i,L}^p = 0, T_{i,L}^p = 0 \ \text{ where}, L \to \infty \end{array}\right\}$$

(21)

Here, the grid points with the X and Y coordinates are represented by the subscripts i and j, respectively, and time $\tau = n\Delta\tau$, $n = 1, 2, 3, 4 \ldots\ldots$

4. Analysis of stability and convergence

The stability and convergence test for this technique is crucial to demonstrate for choosing the appropriate values of the associated parameters because an explicit finite difference procedure will be used to complete this model. For equation (17), stability analysis is not required due to the absence of $\Delta\tau$. First of all, at time $\tau = 0$ we have to consider $e^{i\alpha X}e^{i\beta Y}$ (where, $i = \sqrt{-1}$) as the common term of Fourier expansion. For the dimensionless variables U, θ and φ. However, for any subsequent time, the Fourier expansion formulas for U, θ and φ can be expressed as an equation (22). Additionally, for following the time step $\Delta\tau$, the terms of the Fourier expansion for U, θ and φ and can be recognized in the form of an equation (23).

$$\left.\begin{array}{l} U : S_1\,e^{i\alpha X}e^{i\beta Y} \\ \theta : S_2\,e^{i\alpha X}e^{i\beta Y} \\ \varphi : S_3\,e^{i\alpha X}e^{i\beta Y} \end{array}\right\}$$

(22)

and

$$\left.\begin{array}{l} U' : S_1'\,e^{i\alpha X}e^{i\beta Y} \\ \theta' : S_2'\,e^{i\alpha X}e^{i\beta Y} \\ \varphi' : S_3'\,e^{i\alpha X}e^{i\beta Y} \end{array}\right\}\left(\begin{array}{c}\text{After a time}\\ \text{step}\end{array}\right)$$

(23)

Now, substitute the values of (22) and (23) into equations (18)–(20), and consider U, V as constants. Then the outcome will be as like:

$$S_1' = S_1\left[\begin{array}{l} 1 - \frac{\Delta\tau}{\Delta X}\left(1 - e^{-i\alpha\Delta X}\right)U - \frac{\Delta\tau}{\Delta Y}\left(e^{i\beta\Delta Y} - 1\right)V + \left(1 + \frac{1}{\beta}\right)\frac{2\Delta\tau}{(\Delta Y)^2}(\cos\beta\Delta Y - 1) - \frac{2\Delta\tau Nv}{(\Delta X)^2}(1 - \cos\alpha\Delta X)U^2 \\ \\ -\frac{2\Delta\tau Nv}{(\Delta Y)^2}(\cos\beta\Delta Y - 1)V^2 - \frac{2\Delta\tau Nv}{4\Delta X\Delta Y}UV\{e^{i\alpha(X+\Delta X)}e^{i\beta(Y+\Delta Y)} - e^{i\alpha(X+\Delta X)}e^{i\beta(Y-\Delta Y)}\} \\ \\ +\frac{2\Delta\tau Nv}{4\Delta X\Delta Y}UV\{e^{i\alpha(X-\Delta X)}e^{i\beta(Y+\Delta Y)} - e^{i\alpha(X-\Delta X)}e^{i\beta(Y-\Delta Y)}\} + \Delta\tau M^2\sin^2(\pi X) - \left(1 + \frac{1}{\beta}\right)\Delta\tau Kp \end{array}\right] + \Delta\tau S_2$$

$$+\left(\frac{Gm}{Gr}\right)\Delta\tau S_3$$

(24)

$$S_2^{'} = S_2 \begin{bmatrix} 1 - \frac{\Delta\tau}{\Delta X}U\left(1 - e^{-i\alpha\Delta X}\right) - \frac{\Delta\tau}{\Delta Y}V\left(e^{i\beta\Delta Y} - 1\right) + \frac{\Delta\tau}{(\Delta Y)^2}Nb\left(e^{i\beta\Delta Y} - 1\right)^2\varphi \\ +\frac{1}{Pr}\frac{2\Delta\tau}{(\Delta Y)^2}\left\{1 + Ra(1 + (\theta_w - 1)\theta)^3\right\}(\cos\beta\Delta Y - 1) + \frac{\Delta\tau}{(\Delta Y)^2}Nt\left(e^{i\beta\Delta Y} - 1\right)^2\theta \\ +\frac{Ra}{Pr}(1 + (\theta_w - 1)\theta)^3\frac{\Delta\tau}{(\Delta Y)^2}\left(e^{i\beta\Delta Y} - 1\right)^2 \end{bmatrix}$$
$$+ S_1\left[\left(1 + \frac{1}{\beta}\right)\frac{\Delta\tau Ec}{(\Delta Y)^2}U\left(e^{i\beta\Delta Y} - 1\right)^2 + \Delta\tau EcM^2\sin^2(\pi X)U\right] \tag{25}$$

$$S_3^{'} = S_3\left[1 - \frac{\Delta\tau}{\Delta X}U\left(1 - e^{-i\alpha\Delta X}\right) - \frac{\Delta\tau}{\Delta Y}V\left(e^{i\beta\Delta Y} - 1\right) + \frac{1}{Le}\frac{2\Delta\tau}{(\Delta Y)^2}(\cos\beta\Delta Y - 1) - \Delta\tau Kc(1 + \delta\theta)^n e^{\left(\frac{-AE}{1+\delta\theta}\right)}\right]$$
$$+ S_2\left[\left(\frac{Nt}{Nb\,Le}\right)\frac{2\Delta\tau}{(\Delta Y)^2}(\cos\beta\Delta Y - 1)\right] \tag{26}$$

Subsequently, equations (24)–(26) can be represented as:

$$\left.\begin{array}{l} S_1^{'} = \xi_1\,S_1 + \xi_2\,S_2 + \xi_3\,S_3 \\ S_2^{'} = \xi_4\,S_1 + \xi_5\,S_2 \\ S_3^{'} = \xi_6\,S_2 + \xi_7\,S_3 \end{array}\right\} \tag{27}$$

where,

$$\xi_1 = 1 - \frac{\Delta\tau U}{\Delta X}\left(1 - e^{-i\alpha\Delta X}\right) - \frac{\Delta\tau V}{\Delta Y}\left(e^{i\beta\Delta Y} - 1\right) + \left(1 + \frac{1}{\beta}\right)\frac{2\Delta\tau}{(\Delta Y)^2}(\cos\beta\Delta Y - 1) - \frac{2\Delta\tau NvU^2}{(\Delta X)^2}(1 - \cos\alpha\Delta X)$$
$$- \frac{2\Delta\tau NvUV}{4\Delta X\Delta Y}\left\{e^{i\alpha(X+\Delta X)}e^{i\beta(Y+\Delta Y)} - e^{i\alpha(X+\Delta X)}e^{i\beta(Y-\Delta Y)}\right\} + \frac{2\Delta\tau NvUV}{4\Delta X\Delta Y}\left\{e^{i\alpha(X-\Delta X)}e^{i\beta(Y+\Delta Y)} - e^{i\alpha(X-\Delta X)}e^{i\beta(Y-\Delta Y)}\right\} - \frac{2\Delta\tau NvV^2}{(\Delta Y)^2}(\cos\beta\Delta Y - 1)$$
$$- \Delta\tau M^2\sin^2(\pi X) - \left(1 + \frac{1}{\beta}\right)\Delta\tau Kp$$

$$\xi_2 = \Delta\tau; \; \xi_3 = \left(\frac{Gm}{Gr}\right)\Delta\tau$$

$$\xi_4 = \left(1 + \frac{1}{\beta}\right)\frac{\Delta\tau UEc}{(\Delta Y)^2}\left(e^{i\beta\Delta Y} - 1\right)^2 + \Delta\tau EcUM^2\sin^2(\pi X)$$

$$\xi_5 = 1 - \frac{\Delta\tau}{\Delta X}U\left(1 - e^{-i\alpha\Delta X}\right)$$
$$- \frac{\Delta\tau}{\Delta Y}V\left(e^{i\beta\Delta Y} - 1\right) + \frac{\Delta\tau Nb}{(\Delta Y)^2}\left(e^{i\beta\Delta Y} - 1\right)^{i\beta\Delta Y}\varphi + \frac{1}{Pr}\frac{2\Delta\tau}{(\Delta Y)^2}\left\{1 + Ra(1 + (\theta_w - 1)\theta)^3\right\}(\cos\beta\Delta Y - 1) + \frac{\Delta\tau Nt}{(\Delta Y)^2}\left(e^{i\beta\Delta Y} - 1\right)^2\theta$$
$$+ \frac{Ra}{Pr}(1 + (\theta_w - 1)\theta)^3\frac{\Delta\tau}{(\Delta Y)^2}\left(e^{i\beta\Delta Y} - 1\right)^2$$

$$\xi_6 = \left(\frac{Nt}{NbLe}\right)\frac{2\Delta\tau}{(\Delta Y)^2}(\cos\beta\Delta Y - 1)$$

$$\xi_7 = 1 - \frac{\Delta\tau}{\Delta X}U\left(1 - e^{-i\alpha\Delta X}\right) - \frac{\Delta\tau}{\Delta Y}V\left(e^{i\beta\Delta Y} - 1\right) + \frac{1}{Le}\frac{2\Delta\tau}{(\Delta Y)^2}(\cos\beta\Delta Y - 1) - \Delta\tau Kc(1 + \delta\theta)^n e^{\left(\frac{-AE}{1+\delta\theta}\right)}$$

Moreover, equation (27) can be reorganized in a matrix form as like in equation (28):

$$\begin{bmatrix} S_1^{'} \\ S_2^{'} \\ S_3^{'} \end{bmatrix} = \begin{bmatrix} \xi_1 & \xi_2 & \xi_3 \\ \xi_4 & \xi_5 & 0 \\ 0 & \xi_6 & \xi_7 \end{bmatrix}\begin{bmatrix} S_1 \\ S_2 \\ S_3 \end{bmatrix} \tag{28}$$

Again this system can be rewritten as:

$$\eta^{'} = M^{'}\eta, \text{ where } \eta^{'} = \begin{bmatrix} S_1^{'} \\ S_2^{'} \\ S_3^{'} \end{bmatrix}, M^{'} = \begin{bmatrix} \xi_1 & \xi_2 & \xi_3 \\ \xi_4 & \xi_5 & 0 \\ 0 & \xi_6 & \xi_7 \end{bmatrix}, \text{ and } \eta = \begin{bmatrix} S_1 \\ S_2 \\ S_3 \end{bmatrix}.$$

To determine the eigenvalues of the aforementioned $M^{'}$ matrix, the time step is considered as $\Delta\tau \to 0$. Thus $\xi_2 \to 0, \xi_3 \to 0, \xi_4 \to 0$ and $\xi_6 \to 0$. As a result, $M^{'}$ becomes in form:

$$M^{'} = \begin{bmatrix} \xi_1 & 0 & 0 \\ 0 & \xi_5 & 0 \\ 0 & 0 & \xi_7 \end{bmatrix} \tag{29}$$

So, from equation (29) the eigenvalues of $M^{'}$ are $\lambda_1 = \xi_1, \lambda_2 = \xi_5$ and $\lambda_3 = \xi_7$, where these eigenvalues don't exceed unity in modulus, that is,

$$|\lambda_1| \le 1, |\lambda_2| \le 1, \text{ and } |\lambda_3| \le 1 \tag{30}$$

Furthermore, the supreme modulus of ξ_1, ξ_5 and ξ_7 holds true when $\alpha\Delta X = m^{'}\pi$ and $\beta\Delta X = n^{'}\pi$, where $m^{'}$ and $n^{'}$ refers to odd integers. We have to remember that the value of non-dimensional U is positive and the value of non-dimensional V is negative. Also consider [58–60],

$$A^{'} = \Delta\tau, B^{'} = U\frac{\Delta\tau}{\Delta X}, C^{'} = |-V|\frac{\Delta\tau}{\Delta Y}, D^{'} = \frac{2\Delta\tau}{(\Delta Y)^2}, E^{'} = \frac{2\Delta\tau}{(\Delta X)} \text{ and } F^{'} = \frac{2\Delta\tau}{\Delta\tau\,\Delta Y} \tag{31}$$

So, by implementing these above conditions (equations (30) and (31)), we can express:

$$\xi_1 = 1 - 2\left[B^{'} + C^{'} + \left(1 + \frac{1}{\beta}\right)\left(D^{'} + \frac{A^{'}}{2}Kp\right) - Nv\left(D^{'}V^2 - E^{'}U^2\right) - \frac{Nvf^{'}}{8}UV + \frac{A^{'}}{2}M^2\sin^2(\pi X)\right]$$

$$\xi_5 = 1 - 2\left[B^{'} + C^{'} - D^{'}Nt\,\theta - D^{'}Nb\,\varphi + \frac{1}{Pr}D^{'}\{1 + 2Ra(1 + (\theta_w - 1)\theta)^3\}\right]$$

$$\xi_7 = 1 - 2\left[B^{'} + C^{'} + \frac{1}{Le}D^{'} + \frac{A^{'}}{2}Kc(1 + \delta\theta)^n e^{\left(\frac{-AE}{1+\delta\theta}\right)}\right]$$

The maximum negative bounded values of ξ_1, ξ_5 and ξ_7 are -1. As a result, the stability postulates can be depicted by equations 32–34.

$$U\frac{\Delta\tau}{\Delta X} + |-V|\frac{\Delta\tau}{\Delta Y} + \left(1 + \frac{1}{\beta}\right)\frac{2\Delta\tau}{(\Delta Y)^2} - Nv\left(\frac{2\Delta\tau V^2}{(\Delta Y)^2} - \frac{2\Delta\tau U^2}{(\Delta X)^2} + \frac{\Delta\tau UV}{4\Delta X\Delta Y}\right) + \frac{\Delta\tau}{2}M^2\sin^2(\pi X) + \left(1 + \frac{1}{\beta}\right)\frac{\Delta\tau}{2}Kp \le 1 \tag{32}$$

$$U\frac{\Delta\tau}{\Delta X} + |-V|\frac{\Delta\tau}{\Delta Y} + \frac{1}{Pr}\frac{2\Delta\tau}{(\Delta Y)^2}\left[1 + 2Ra\{1 + (\theta_w - 1)\theta\}^3\right] - Nb\frac{2\Delta\tau}{(\Delta Y)^2}\varphi - Nt\frac{2\Delta\tau}{(\Delta Y)^2}\theta \le 1 \tag{33}$$
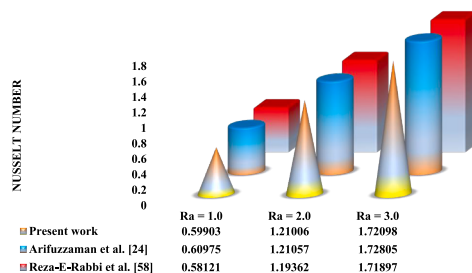

Fig. 4. Comparative bar diagrams for code validation of Nusselt number.

$$U\frac{\Delta\tau}{\Delta X}+|-V|\frac{\Delta\tau}{\Delta Y}+\frac{1}{Lc}\frac{2\Delta\tau}{(\Delta Y)^2}+\frac{\Delta\tau}{2}Kc(1+\delta\theta)^n e^{\left(\frac{-AE}{1+\delta\theta}\right)}\leq 1 \tag{34}$$

And here, $U=0, V=0, \theta=0, \varphi=0$ at $\tau=0$ are the key boundary conditions. For $\Delta\tau=0.0005$, $\Delta X=0.2$, and $\Delta Y=0.2$, the convergence conditions for this particular study would be founded as $Pr\geq 0.075$, and $Le\geq 0.041$.

5. Code validation

In order to validate the assessment and meticulously scrutinize the precision of the present findings, a meticulous comparative numerical analysis has been conducted in juxtaposition with the seminal works of Arifuzzaman et al. [24] and Reza-E-Rabbi et al. [58]. Additionally, a numerical contrast of the heat transfer factor field has been artfully represented through a bar chart (Fig. 4). When Ra = 3, the error percentages are 0.12 % and 0.41 % in comparison to Refs. [24,58]. This depiction unequivocally signifies the strong congruence between the most recent results and their antecedents. Furthermore, it merits mention that we have undertaken the experimental confirmation of the applied EFD procedure in the very recent past.

6. Results and discussion

To explore the physical phenomena of this problem, a numerical solution is obtained by using a straightforward explicit finite difference procedure. The numerical values of non-dimensional velocity, temperature, and concentration within the boundary layer for altered values of non-dimensional parameters have been calculated by using EFDM. We have discussed our numerical solutions graphically. In Figs. 5–24, the effects of the associated physical parameters on the dimensionless velocity, temperature, and concentration are explained. In general, the selected values of these parameters are as follows: $Nv=0.2$, $\beta=0.5$, $M=4.0$, $Gm=1.0$, $Gr=5.0$, $Kp=1.0$, $Pr=1.0$, $Ra=2.0$, $Ec=0.01$, $Nb=0.3$, $Nt=0.5$, $Kc=0.2$, $Le=5.0$, $AE=2.0$, $\delta=1.0$, $\theta_w=1$ and 0.6.

6.1. Significance of velocity field

In the following Figs. 5–6, the consequences of magnetic field (M) is shown on the velocity distribution (U) for both Casson and Maxwell fluid for both linear ($\theta_w=1$) and nonlinear ($\theta_w=0.6$) thermal radiation. It is discovered that higher values of magnetic field caused the velocity profiles to steadily decrease. Fig. 5 indicates the dissimilarity of the velocity field against the greater value of M for linear thermal radiation, where the velocity profile reduces. With the intensification of magnetic field, Lorentz forces produces in the fluid domain. These Lorentz forces produce more resistance for this fluid flow. As a result, velocity decays consequently for both Casson and Maxwell fluid. Moreover, it is clear form this figure that the effect of Casson fluid is stronger than Maxwell fluid for the case of linear thermal radiation. On the other hand, Fig. 6 represents that the velocity field for nonlinear thermal radiation of this fluid model which is little bit different than linear thermal radiation case. In this case the effect of Maxwell fluid on velocity profile is more than Casson fluid for nonlinear radiation.
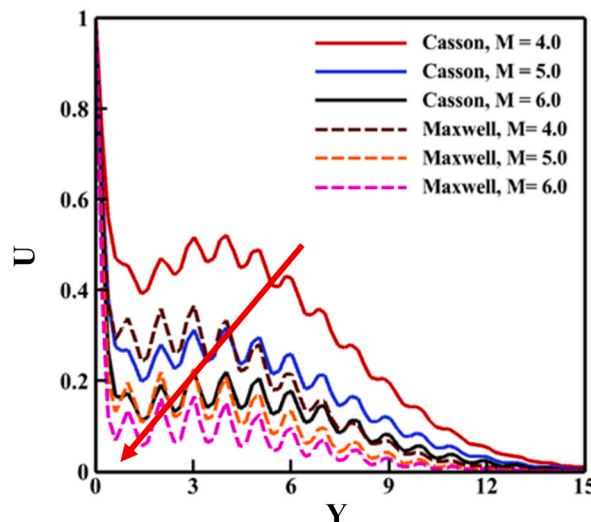

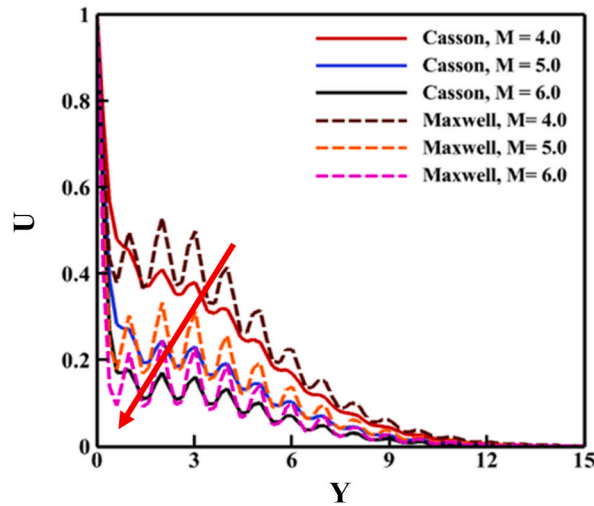**Fig. 5.** Influence of M on U for linear radiation.

Fig. 6. Influence of M on U for nonlinear radiation.
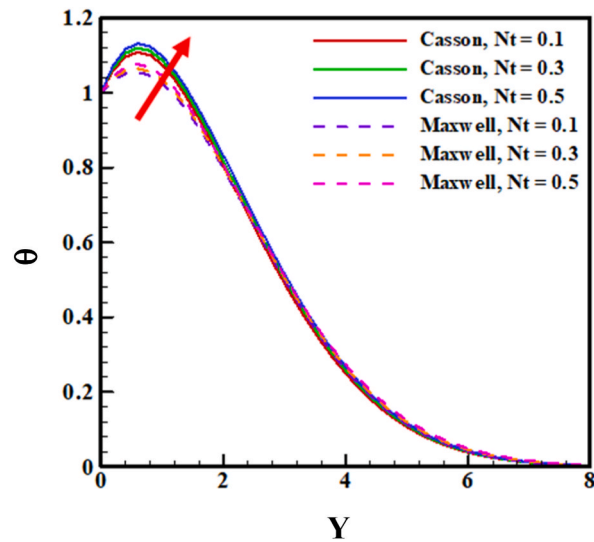

Fig. 7. Influence of Nt on θ for linear radiation.

6.2. Significance of thermal energy

Figs. 7–12 display the temperature distribution of Casson and Maxwell fluids for dissimilar values of thermophoresis factor (Nt), Brownian motion parameter (Nb), and thermal radiation parameter (Ra) for both cases of linear and nonlinear thermal radiation. It is clear that due to the upsurge of Nt, Nb and Ra, the temperature profile gradually shows enhancement for both Casson and Maxwell fluids.

Mathematically in Figs. 7 and 8, due to the escalation of Nt, the thermophoretic force also upsurge. As a result, this force causes nanoparticles to migrate in the opposite direction as the temperature differential. For this incidence, the temperature of the entire domain is raised for Casson and Maxwell fluids. But it is clear from Fig. 7, for linear thermal radiation the effect of Casson fluid is stronger than Maxwell fluid in this fluid model. Moreover, a similar impact is also seen for the increased value of the thermophoretic force (Nt) for nonlinear thermal radiation case on temperature field in Fig. 8. In that time, the change of fluid temperature is faster for nonlinear thermal radiation than linear thermal radiation case for both Casson and Maxwell fluids. Finally, from Figs. 7 and 8, for both cases of Casson and Maxwell fluids, it is clear that nonlinear thermal radiation has a better impact than linear thermal radiation on this fluid's temperature profile.

In addition to, a similar impact is also seen for Casson and Maxwell fluids in Figs. 9 and 10 for the increased value of Nb. For increasing value of Brownian motion, nanoparticles motion is becoming stimulated. As a result, Nb supports an upsurge in temperature distribution. In Fig. 9, the effect of Casson and Maxwell fluid on temperature field is shown for linear thermal radiation case. In that
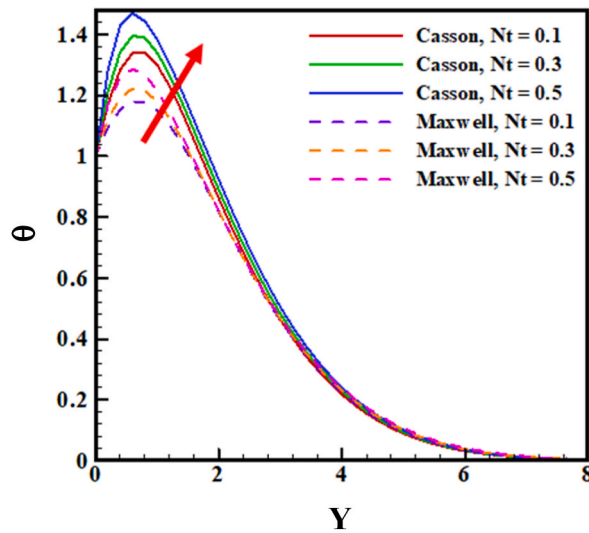
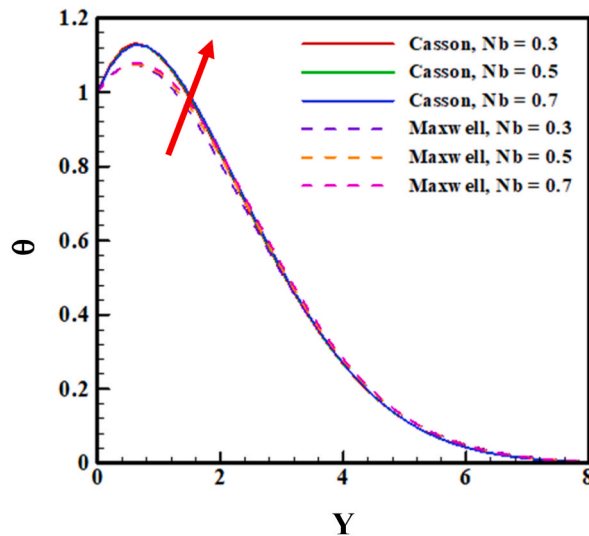**Fig. 8.** Influence of *Nt* on θ for nonlinear radiation.

Fig. 9. Influence of *Nb* on θ for linear radiation.

case, the temperature changing (increase) behavior for both fluid as like similar. On the other hand, in Fig. 10, the effect of Casson and Maxwell fluid on temperature field is shown for nonlinear thermal radiation case. In that time, the temperature changing behavior is faster for both of these fluids. Also, for Casson fluid, this behavior become stronger than Maxwell fluid. Finally, from Figs. 9 and 10, for both cases of Casson and Maxwell fluids, it is clear that nonlinear thermal radiation has a better impact than linear thermal radiation on this fluid's temperature profile.

Additionally, a comparable influence is observed in Figs. 11 and 12 for elevated *Ra* values in the context of Casson and Maxwell fluids. The escalation in temperature due to the augmentation of thermal radiation intensity stems from the Stefan-Boltzmann law, elucidating the connection between an object's temperature and the magnitude of radiation it emits. As an object emits more radiation due to heightened temperature, it expends energy at an accelerated rate, leading to an energy incongruity that is commonly rectified by absorbing additional energy from its surroundings, consequently amplifying its temperature. In Fig. 11, the impact of Casson and Maxwell fluids on the temperature field is demonstrated in the scenario of linear thermal radiation.

In this scenario, the alteration in temperature behavior for both fluids appear analogous. In contrast, in Fig. 12, the temperature field's response to Casson and Maxwell fluids is exhibited under conditions of nonlinear thermal radiation. On this occasion, the alteration in temperature behavior is swifter for both fluids. Moreover, for the Casson fluid, this effect becomes more pronounced than for the Maxwell fluid. Ultimately, discernible from Figs. 11 and 12, it becomes evident that nonlinear thermal radiation exerts a more favorable influence than linear thermal radiation on the temperature distribution of these fluids.
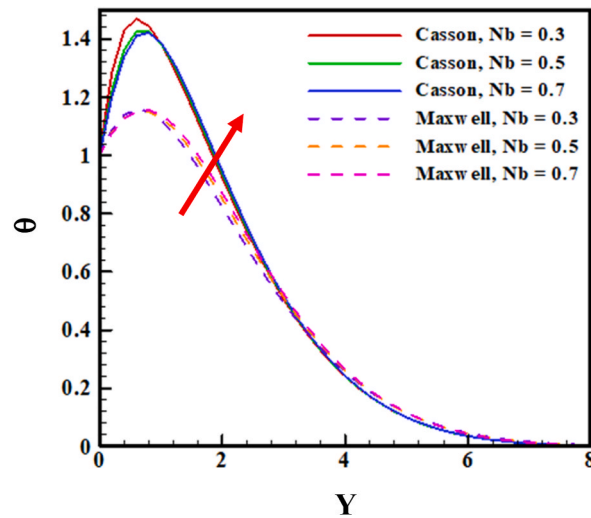
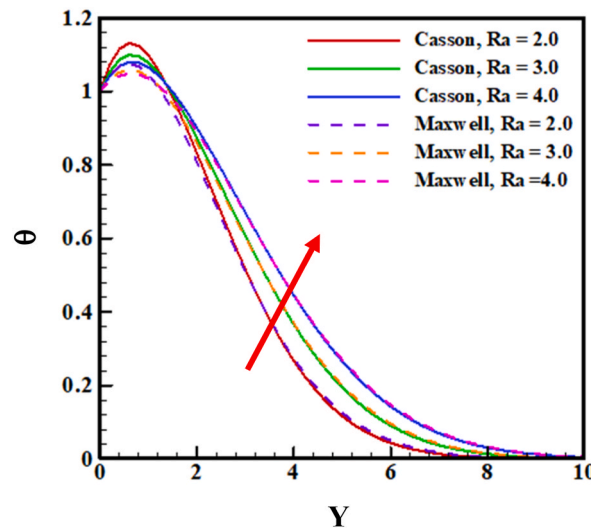**Fig. 10.** Influence of Nb on θ for nonlinear radiation.

Fig. 11. Influence of Ra on θ for linear radiation.

6.3. Significance of concentration field

In addition to, Figs. 13–16 displays the concentration distribution with ($AE = 1$) and without Arrhenius activation energy ($AE = 0$) for different values of chemical reaction parameter (Kc). From Figs. 13 and 14, we observed that the concentration profile decreases for both cases, i.e. with activation energy ($AE = 1$) and without activation energy ($AE = 0$) for rising values of chemical reaction parameter (Kc). Clearly, it is noticed that with the increase of the value of Kc, the concentration profile diminished with the higher values of Kc, and when activation energy is included ($AE = 1$), the chemical reaction parameter has a more significant.

Furthermore, a similar impact is noted in Figs. 15 and 16 for increased AE values in the context of Casson and Maxwell fluids. Higher activation energy typically results in slower reaction rates, leading the rate of reactant consumption to be outpaced by production or inflow due to the stretched sheet's border constraints. This leads to reactant accumulation and consequent concentration augmentation.

In Fig. 15, the influence of Casson and Maxwell fluids on concentration fields is portrayed in the scenario of non-linear thermal radiation. On this occasion, the change in concentration behavior is more rapid for both fluids. In contrast, Fig. 16 illustrates the concentration field response of Casson and Maxwell fluids under conditions of linear thermal radiation. Here, the change in concentration behavior for both fluids appear analogous. Moreover, this effect is notably more pronounced for the Casson fluid compared to the Maxwell fluid. Ultimately, discerned from Figs. 15 and 16, it becomes evident that non-linear thermal radiation yields a more favorable impact on the concentration distribution of these fluids compared to linear thermal radiation.
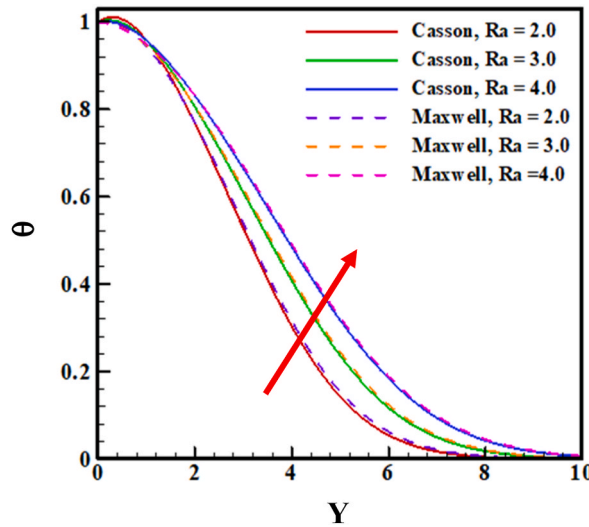
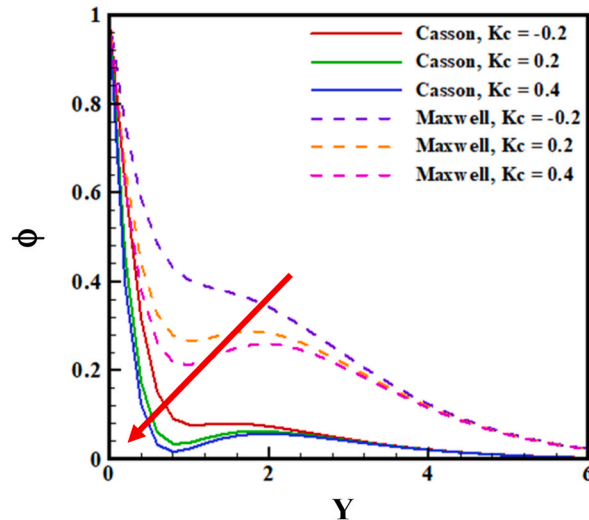**Fig. 12.** Influence of *Ra* on *θ* for nonlinear radiation.

Fig. 13. Influence of *Kc* on *φ* for with activation energy.

6.4. Significance of stream lines

Here, Figs. 17–20 delineate the streamlines of Casson fluids and Maxell fluids, delineating a spectrum of activation energy (*AE*) values within the frameworks of linear and nonlinear thermal radiation. It becomes patently clear that with the ascending *AE* values, there emerges a gradual amplification discernible in the streamlines of both fluids flow, i.e. Casson fluid and Maxwell fluid, as eloquently showcased in the graphical illustration presented for Casson fluids within Fig. 18, while a more sophisticated visualization is thoughtfully presented in Fig. 17. On the other hand, for Maxwell fluids the line view is drawn in Fig. 20 and flood view in Fig. 19.

6.5. Significance of isothermal lines

The isothermal lines of Casson fluids are shown in Figs. 21–24, together with a range of values for thermal radiation (*Ra*) within the contexts of linear and nonlinear thermal radiation.

As eloquently demonstrated in the graphical representation provided in Fig. 22, a more complex visualization is thoughtfully presented in Fig. 21 for Casson fluids, while the flood view of the isothermal lines and line view have been portrayed in Figs. 23 and 24, respectively. It is evidently obvious that with the ascending *Ra* values, there grows an upward enhancement identifiable in the isothermal lines for both fluids (Casson fluids and Maxwell fluids).
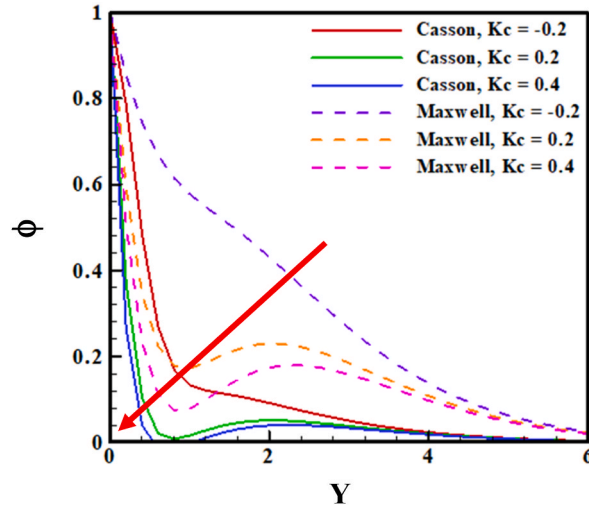
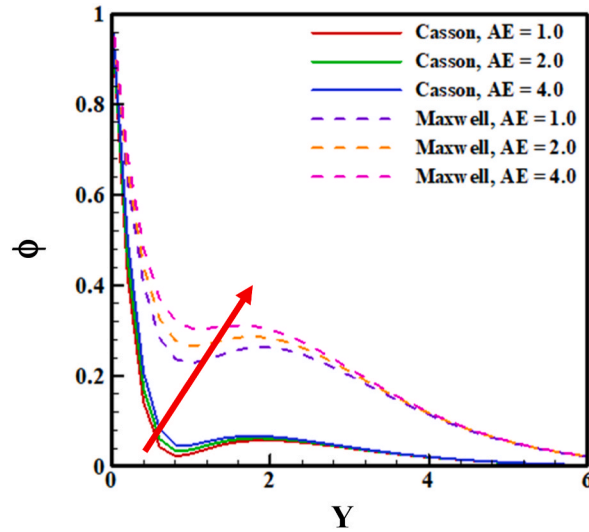**Fig. 14.** Influence of *Kc* on *φ* for without activation energy.

Fig. 15. Effect of activation energy (*AE*) on concentration profile for nonlinear thermal radiation.

6.6. Response surface methodology

To study how the input factors (*Nt*, *Nb*, and *Ra*) act on the Nusselt number (*Nu*) for this Casson-Maxwell nanofluid model, the response surface methodology (RSM) is applied. According to Montgomery [61], RSM is a valuable technique that can be used to model multivariate situations. The second-order RSM model that accounts for all linear, square, and interaction components is often appropriate to estimate the response, despite the circumstance that there are alternative RSM models existing. The quadratic polynomial model is provided by the following:

$$y = c_0 + \sum_{i=1}^{3} c_i x_i + \sum_{i=1}^{3} c_{ii} x_i^2 + \sum_{i=1}^{3} c_{ij} x_i x_j \tag{35}$$

where *y* is the response function (output), c_0 is the intercept, c_i is the linear regression coefficient of *i*th factor, c_{ii} is the coefficient of quadratic regression of *i*th factor, c_{ij} is the interaction of *i*th and *j*th factors. Here, the significant parameters *Nt*, *Nb* and *Ra* are taken as input factors whereas Nu_{ca} (Nusselt number for Casson fluid) and Nu_{max} (Nusselt number for Maxwell fluid) are considered as response faction (*y*). By maximizing the value of variable *y*, the objective is to create an appropriate correlation between the independent factors and the response function. A central composite design (CCD), first proposed by Box and Wilson [62] in 1992, and was utilized to convey the second-order model. Currently, it is the utmost widely used subset of designs. Furthermore, in this design, the input
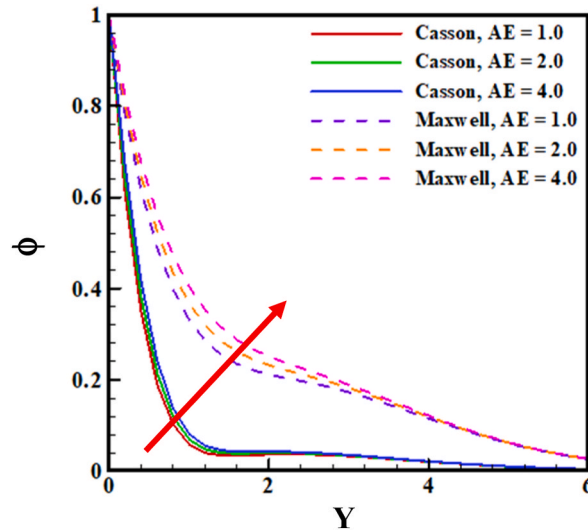
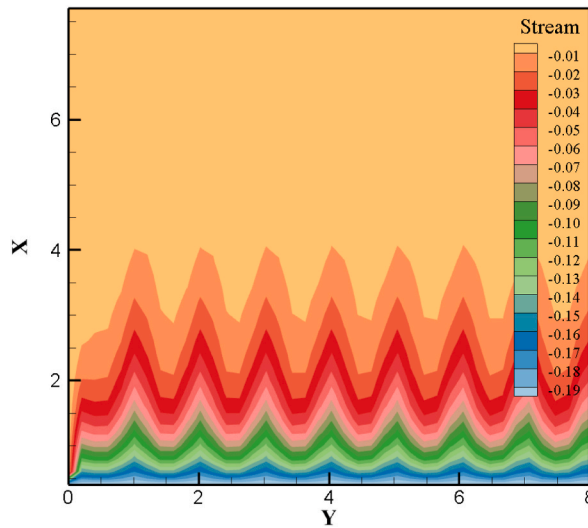**Fig. 16.** Effect of activation energy (*AE*) on concentration profile for linear thermal radiation.

Fig. 17. Stream lines of Casson fluids against activation energy *AE*.

variables' range *Nb*, *Nt* and *Ra* are $0.1 \leq Nb \leq 0.7, 0.1 \leq Nt \leq 0.7$ and $1 \leq Ra \leq 3$. Here, in total 20 runs (points) are taken according to three factors CCD, and these are sub classified as 6 axials, 6 center and 8 cube points. Table 1 provides a description of the codded levels of the input factors. And Table 2 also shows the simulation run setups for coded and real data created by CCD.

Table 3 and Table 4 display the statistical results of average Nusselt number for Maxwell fluid (*Nu_max*) and Casson fluid (*Nu_ca*) by means of RSM. In these Tables, this model's greatest quantity of independent elements is represented by the degrees of freedom (DOF). A method for representing the total dissimilarity resulting from numerous factors is the sum of squares (SS) which is quite substantial. The indication of F-value denotes this model of *Nu_max* and *Nu_ca* are statistically substantial. Additionally, the p-value, which indicates the probability occurring null hypothesis hold true for a certain model, is a highly significant indicator of this statistical study. To put it another way, a very little p-value (usually 0.05) point to the model is suitable. Additionally, strong values of the R^2, 99.9 % for *Nu_max* and 88.98 % for *Nu_ca*, are suggested that the statistical analysis is quite significant for this model. Lack-of-Fit is another crucial indicator as well, and it must be very little for a model to be effective. For both cases, the Lack-of-Fit is insignificant.

The general best fitted regression model that RSM created is shown in equation (35). It was created to examine the connection between the response function *y* (*Nu_max* and *Nu_ca*) with the involved input parameters N_b, N_t and R_a:

$$y\left(Nu_{\max}, Nu_{ca}\right) = c_0 + c_1 Nb + c_2\, Nt + c_3\, Ra + c_{11}Nb^2 + c_{22}\, Nt^2 + c_{33}\, Ra^2 + c_{12}Nb.Nt + c_{13}Nb.Ra + c_{23}\, Nt.Ra \tag{36}$$

where $c_0, c_1, c_2, c_3, c_{11}, c_{22}, c_{33}, c_{12}, c_{13}$ and c_{23} are coefficients to make an appropriate (best-fitted) regression model. Additionally,
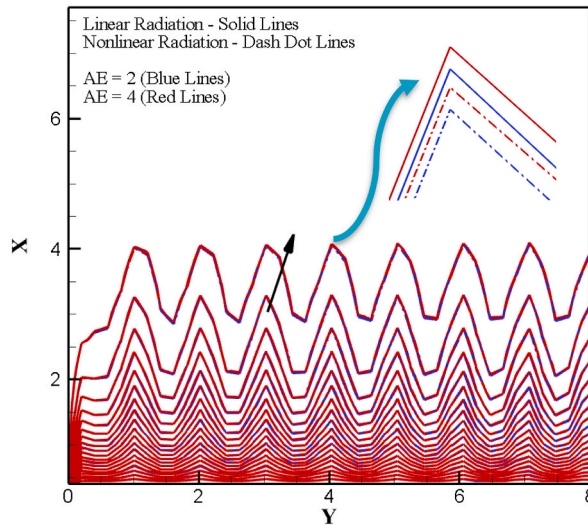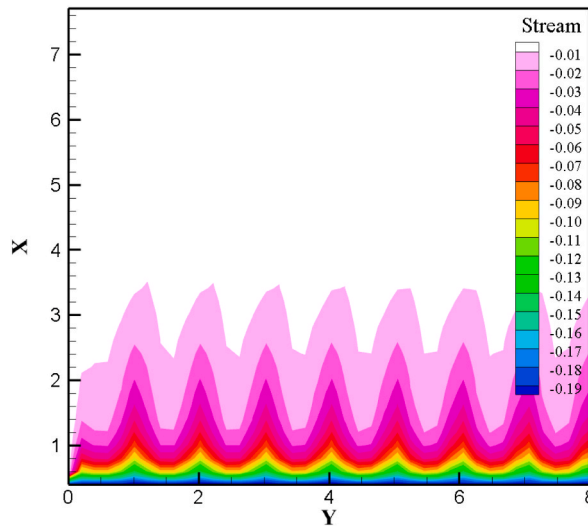
Fig. 18. Line view of Fig. 17.

Fig. 19. Stream lines of Maxwell fluids against activation energy *AE*.

the projected coefficients of equation (35) for Nu_{max} are included in Table 5, which are generated as coded units. Similarly, the projected coefficients for the best fitted regression model of Nu_{ca} are included in Table 6. Because of their importance, only the significant model terms with low p-values (less than 5 %) have been used to construct a suitable regression equation. On the other hand, useless terms (bold indicated) have been disregarded.

That is, the term Nb^2 is totally insignificant for the regression equation (35) of Nu_{max}. Similarly, the terms $Nt^2, Nb \cdot Nt$ and $Nt \cdot Ra$ must be omitted to create a best fitted regression model for Nu_{ca}. So, the relation between the response functions (Nu_{max}, Nu_{ca}) and the input variables (Nb, Nt, and Ra) may therefore be summarized mathematically using the following correlations respectively:

$$Nu_{max} = 1.726 - 0.0545\,Nb - 0.0907Nt + 0.3396\,Ra - 0.0042Nt^2 + 0.0394\,Ra^2 - 0.0045\,Nb.Nt + 0.0039Nb.Ra + 0.0082\,Nt.Ra \quad (37)$$

$$Nu_{ca} = 1.678 - 0.0718\,Nb - 0.3984Nt + 0.2432\,Ra - 0.4056Nt^2 + 0.0733\,Ra^2 - 0.3365Nb\,.Ra \quad (38)$$

6.7. Response surface analysis

To visualize the influence of effective parameters on Nu_{max}, the 2D and 3D contour plots obtained by using RSM of response surface are described in Figs. 25–27. The impact of Nb and Nt on the response function is seen in Fig. 25(a). This 2D contour map makes it evident that as Nb and Nt are increased, the Nusselt number for Maxwell fluid (Nu_{max}) decreases while Ra remains constant. For
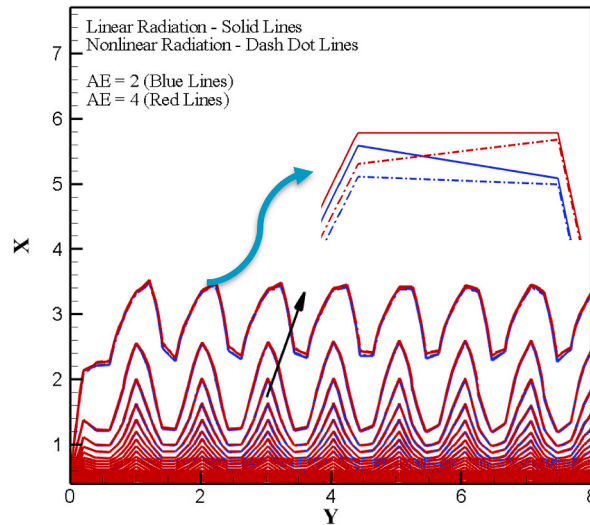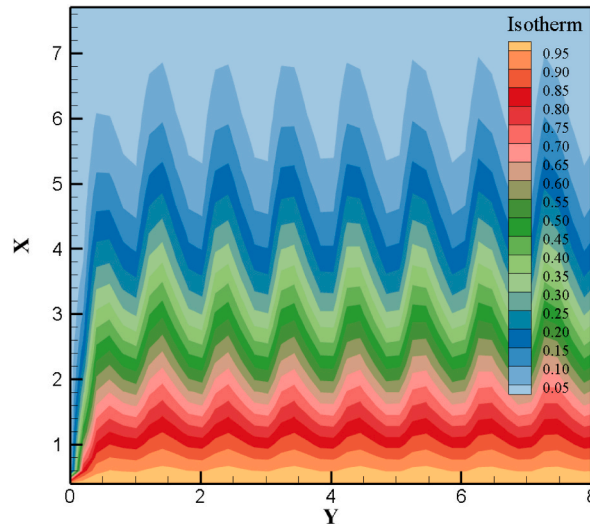
Fig. 20. Line view of Fig. 19.

Fig. 21. Isothermal lines of Casson fluids against radiation *Ra*.

example, the value of *Nb* and *Nt* are raised to 0.4 from 0.1, the rate of Nusselt number for Maxwell fluid is decreased by 18.57 %. Also, for $Nb = Nt = 0$, the Nu_{max} shows the highest value.

Additionally, Fig. 25(b) depicts a 3D surface view for observing the impacts of *Nb* and *Nt* on Nu_{max}. Fig. 26 once more displays the Nu_{max} oscillations with *Nb* and *Ra*. In Figs. 26(a) and (b), when *Ra* is increased but *Nb* is decreased, the Nu_{max} intensifications by holding another factor (*Nt*) as constant. Furthermore, Fig. 27 expresses yet another 2D and 3D graphical representations to represent impact of response function Nu_{max} for Maxwell fluid. Also, the rate of Nu_{max} is improved due to the boosted of *Ra* but diminish the *Nt*. On the other hand, using RSM the impression of effective factors on Nu_{ca} is described by 2D and 3D contour plots that are given in Figs. 28–30. The control of *Nb* and *Nt* on the response Nu_{ca} is seen in Fig. 28 (a) by a 2D contour plot. This 2D contour map makes it evident that when the value of *Nb* and *Nt* are enlarged, the Nu_{ca} decreases. It is noticeable that the impact of nonlinear thermal radiation (*Ra*) is clearly visualize on response surface by the contour lines. Rather than the Maxell fluid, this impact of nonlinearity about *Ra* is greater for Casson fluid. Again, Fig. 28(b) depicts a 3D surface view to visualize this impact clearly. In similar manner, Fig. 29(a) and (b) depict the consequence of *Nb* and *Ra* on the response function Nu_{ca} in 2D and 3D perspective. Also, the influence of the *Nt* and *Ra* on the rate of Nusselt number for Casson fluid (Nu_{ca}) is described in Figs. 30(a) and 30(b). In both Figs. 29 and 30, it is clearly noticeable that the *Ra* has a greater impact on the average heat transfer rate of Casson fluid.
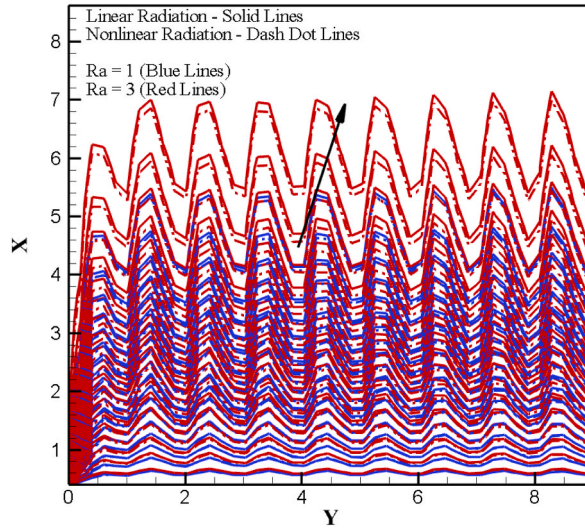
Fig. 22. Lines view of Fig. 21.
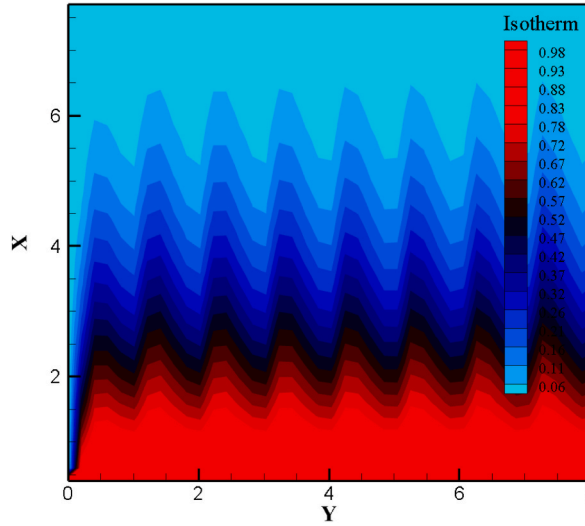
Fig. 23. Isothermal lines of Maxwell fluids against radiation *Ra*.

6.8. Sensitivity analysis

Sensitivity analysis, a method for measuring the amount of significant levels on output, is a key component of numerical simulation. Performing a "sensitivity analysis" to regulate how the RSM model's parameter values affect the resultant variables is another definition of the term [63]. The most effective parameter can be found by ranking the input factors according to their influence. Mathematically, the partial derivatives of the response functions are used to determine the output variables' sensitivity to effective input factors (*Nb*, *Nt*, and *Ra*). This leads to the computation of the response function Nu_{max} which is equation (36) to the input parameters as follows:

$$\frac{\partial Nu_{\max}}{\partial Nb} = -0.0545 - 0.0045 Nt + 0.0039 Ra \tag{39}$$

$$\frac{\partial Nu_{\max}}{\partial Nt} = -0.0907 - 0.0084 Nt - 0.0045 Nb + 0.0082 Ra \tag{40}$$

$$\frac{\partial Nu_{\max}}{\partial Ra} = 0.3396 + 0.0788 Ra + 0.0039 Nb + 0.0082 Nt \tag{41}$$

Fig. 24. Line view of Fig. 23.

Table 1
Input factors and codded levels for CCD.

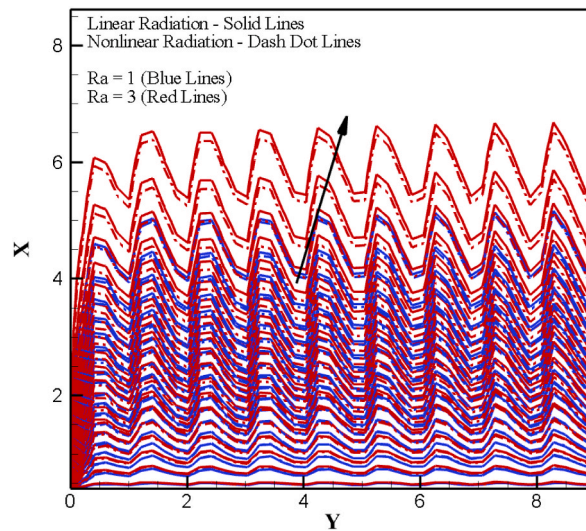| Variables Name	Level		
	−1 (lowest)	0 (medium)	1 (highest)
Nb	0.1	0.4	0.7
Nt	0.1	0.4	0.7
Ra	1	2	3

Table 2
Values of factors and response.

Run Order	Codded values			Actual Values			Response function	
	Nb	Nt	Ra	Nb	Nt	Ra	Nu_{max}	Nu_{ca}
1	0	0	0	0.4	0.4	2	1.15505	1.23589
2	−1	0	0	0.1	0.4	2	1.16986	1.24009
3	0	−1	0	0.4	0.1	2	1.17871	1.25571
4	0	0	0	0.4	0.4	2	1.15505	1.23589
5	0	1	0	0.4	0.7	2	1.13063	1.21539
6	0	0	0	0.4	0.4	2	1.15505	1.23589
7	1	1	−1	0.7	0.7	1	1.32839	1.40699
8	0	0	1	0.4	0.4	3	1.01718	1.1116
9	−1	−1	−1	0.1	0.1	1	1.41293	1.45836
10	−1	1	1	0.1	0.7	3	1.00945	1.51096
11	−1	−1	1	0.1	0.1	3	1.05146	1.52984
12	0	0	0	0.4	0.4	2	1.15505	1.23589
13	1	−1	1	0.7	0.1	3	1.02482	1.12592
14	0	0	−1	0.4	0.4	1	1.37173	1.43319
15	−1	1	−1	0.1	0.7	1	1.36136	1.41631
16	0	0	0	0.4	0.4	2	1.15505	1.23589
17	1	−1	−1	0.7	0.1	1	1.38189	1.44954
18	1	0	0	0.7	0.4	2	1.14003	1.23167
19	0	0	0	0.4	0.4	2	1.15505	1.23589
20	1	1	1	0.7	0.7	3	0.98146	1.08901

Now, the response function's (Nu_{max}) sensitivity results, in Table 7, to the input variables Nb, Nt, and Ra may be calculated using equations (38)–(40). With Nb at levels of −1, 0 and 1 (0.1, 0.4, 0.7), Nt at levels of −1 (0.1), and Ra at levels 0 and 1 (2 and 3), these values were derived using the model. Here, a negative sensitivity indicates completely the opposite effect, where the increasing value of input factors leads to decrease the output. That is, the Nb and Nt have negative impact on the heat transfer rate for Maxwell fluid. A positive sensitivity, on the other hand, denotes that increasing the input factors causes develop the response. Therefore, the radiation parameter (Ra) has a favorable effect on the Nu_{max}.

Table 3
Analysis of variance for Nu_{max}.

Source	DOF	SS	F-Value	p-Value	Comment
Model	9	0.3296	2.3×10^6	<0.0001	**Significant**
Nb	1	0.0022	1.3×10^5	<0.0001	
Nt	1	0.0057	3.5×10^5	<0.0001	
Ra	1	0.3140	1.9×10^7	<0.0001	
Nb. Nb	1	3.03×10^{-8}	1.91	**0.1971**	
Nt. Nt	1	3.97×10^{-7}	25.01	0.0005	
Ra. Ra	1	0.0043	2.6×10^6	<0.0001	
Nb. Nt	1	1.34×10^{-6}	84.7	<0.0001	
Nb. Ra	1	0.0001	692.66	<0.0001	
Nt. Ra	1	0.0001	3033.25	<0.0001	
Lack-of-Fit	5	1.5×10^{-7}	-	-	**Insignificant**
Pure Error	5	0.000	-	-	

**Here, $R^2 = 99.99$ %, Adjusted $R^2 = 99.9$ %.

Table 4
Analysis of variance for Nu_{ca}.

Source	DOF	SS	F-Value	p-Value	Comment
Model	9	0.3019	8.97	0.0010	**Significant**
Nb	1	0.0727	19.44	0.0013	
Nt	1	0.0033	17.35	0.0372	
Ra	1	0.0635	16.99	0.0021	
Nb. Nb	1	0.0037	0.9981	**0.3413**	
Nt. Nt	1	0.0816	0.9802	0.0345	
Ra. Ra	1	0.0037	3.96	0.0347	
Nb. Nt	1	0.0001	0.0115	**0.9168**	
Nb. Ra	1	0.0816	21.82	0.0009	
Nt. Ra	1	0.0001	0.0278	**0.8710**	
Lack-of-Fit	5	0.0374	-	-	**Insignificant**
Pure Error	5	0.000	-	-	

**Here, $R^2 = 88.98$ %, Adjusted $R^2 = 79.06$ %.

Table 5
Regression coefficients for Nu_{max} that are predicted based on RSM.

Coefficients	c_0	c_1	c_2	c_3	c_{11}	c_{22}	c_{33}	c_{12}	c_{13}	c_{23}
Values	1.726	−0.0545	−0.0907	−0.138	−0.0011	−0.0042	0.0394	−0.0045	0.0039	0.0082
p-values	–	<0.0001	<0.0001	<0.0001	**0.1971**	0.0005	<0.0001	<0.0001	<0.0001	<0.0001

Table 6
Regression coefficients for Nu_{ca} that are predicted based on RSM.

Coefficients	c_0	c_1	c_2	c_3	c_{11}	c_{22}	c_{33}	c_{12}	c_{13}	c_{23}
Values	1.678	0.0718	−0.3984	−0.2432	0.4092	0.4056	0.0733	−0.0257	−0.3365	0.0120
p-values	–	0.0013	0.0372	0.0021	**0.3413**	0.0345	0.0347	**0.9168**	0.0009	**0.8710**

Thus, the Nu_{max} is negatively sensitive by the Nb and Nt that is described in Table 7. Therefore, the rate of heat transmission for this Maxwell fluid must decrease as Nb and Nt increase. Conversely, the Ra has a positive sensitivity on Nu_{max}. So, with the improvement of Ra, the response function changed positively. Additionally, the vertical bar in Fig. 31 symbolizes positive sensitivity, while the downward bar reflects negative sensitivity about Nu_{max}. The entire length of the bar diagram indicates the sensitivity level. From this it is concluded that the rate of sensitivity of Ra on this Maxwell fluid is the highest rather than others two parameter (Nb and Nt).

In similar manner, by taking partial derivatives of the response function Nu_{ca} with respect to input parameters (Nb, Nt, and Ra) from equation (37) we get as follows:

$$\frac{\partial Nu_{ca}}{\partial Nb} = -0.0718 - 0.0035Ra \tag{42}$$

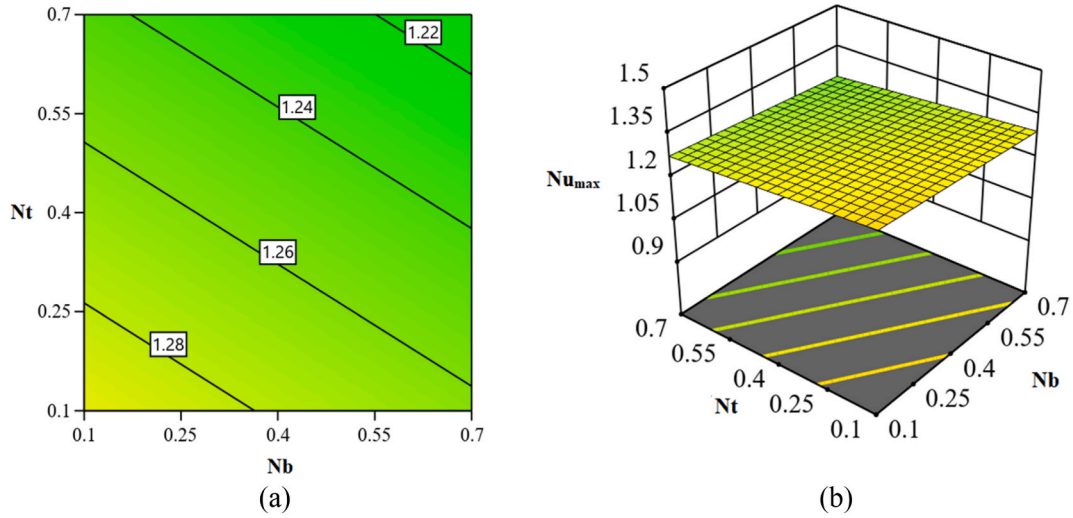$$\frac{\partial Nu_{ca}}{\partial Nt} = -0.3984 + 0.8112Nt \tag{43}$$

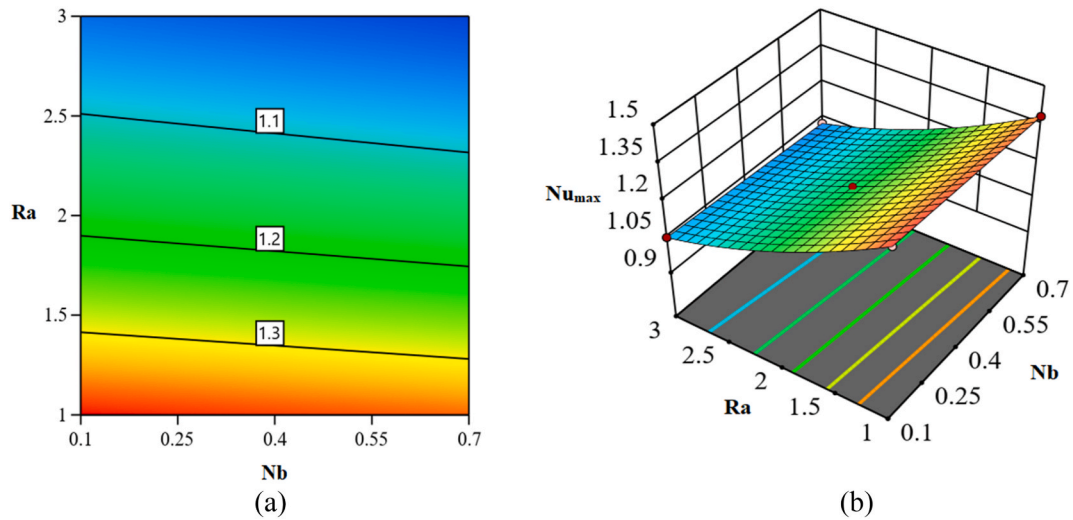**Fig. 25.** Effect of Nu_{max} for Nb and Nt: (a) 2D and (b) 3D eyesight.

Fig. 26. Effect of Nu_{max} for Nb and Ra: (a) 2D and (b) 3D eyesight.

$$\frac{\partial Nu_{ca}}{\partial Ra} = 0.2432 + 0.1466Ra - 0.3365Nb \tag{44}$$

Again, the sensitivity results of Nu_{ca} for Nb, Nt, and Ra may be calculated using equations (41)–(43). With Nb at levels of -1, 0 and 1 (0.1, 0.4, 0.7), Nt at levels of -1 (0.1), and Ra at levels 0 and 1 (2 and 3), these values are derived using the model. The Nb and Nt have negative impact on the heat transfer rate for the Casson fluid. Here, Nu_{ca} is negatively sensitive by the Nb and Nt that is described in Table 8. Conversely, also the Ra has a positive sensitivity on Nu_{ca}. So, with the improvement of Ra, the response function changed positively. Similarly, the vertical bar in Fig. 32 symbolizes positive sensitivity, while the downward bar reflects negative sensitivity about Nu_{ca}. From this table and figure, it is concluded that the rate of sensitivity of Ra on this Casson fluid is the highest rather than others two parameter (Nb and Nt).

7. Conclusions

In this portion, an exploration ensues into the dynamic characteristics of periodic magneto-hydrodynamic Casson and Maxwell fluids, specifically addressing the interplay of heat and mass transfer mechanisms amid the influences of nonlinear radiation and Arrhenius activation energy. The examination is directed towards the scenario of a stretching sheet. Employing an explicit finite difference methodology, a numerical solution is constructed to encapsulate the intricate behavior. The response surface approach,
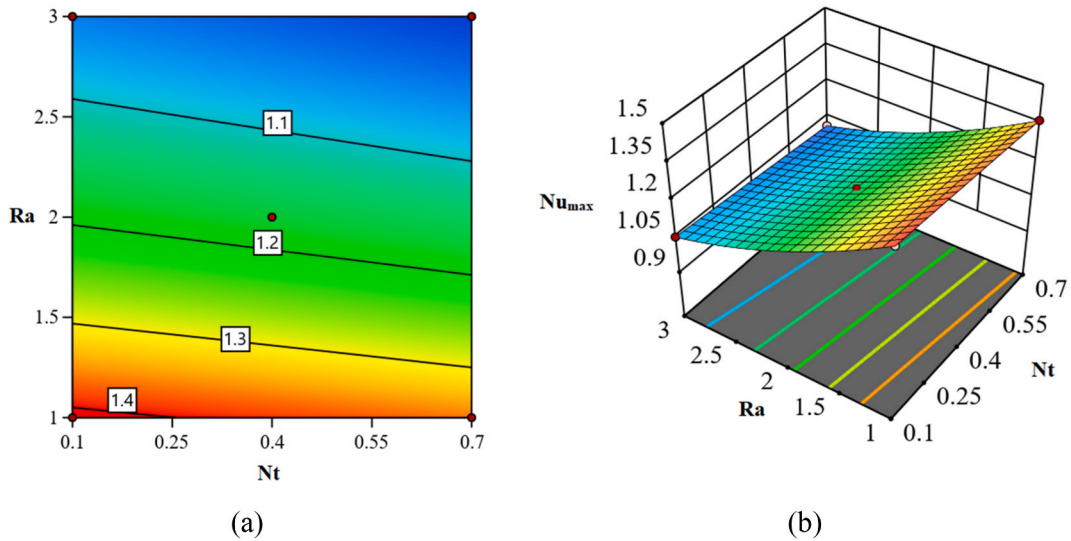
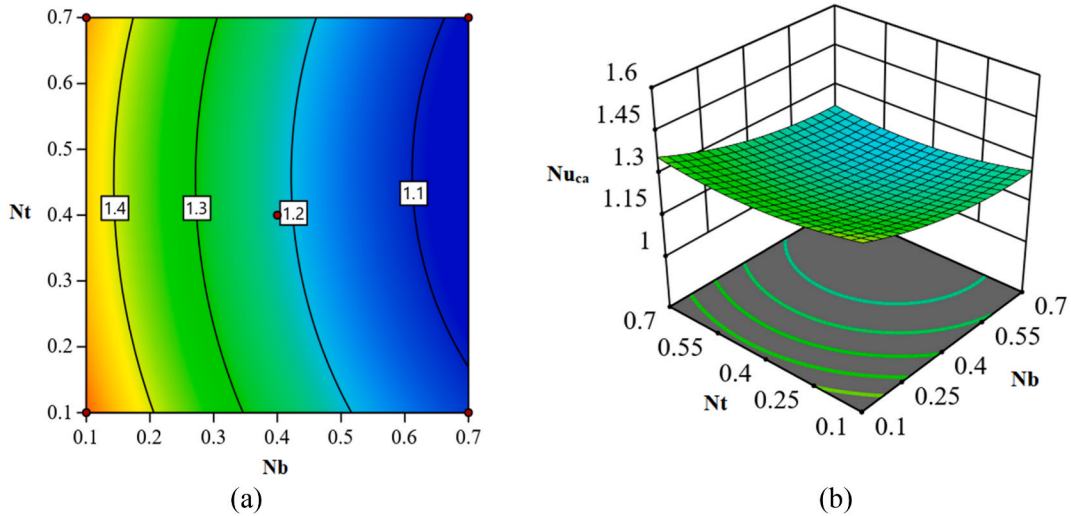**Fig. 27.** Effect of Nu_{max} for Nb and Ra: (a) 2D and (b) 3D eyesight.

Fig. 28. Effect of Nu_{ca} for Nb and Nt: (a) 2D and (b) 3D eyesight.

response surface analysis, and sensitivity analysis are only a few of the methods used for in-depth investigation. These investigations explore the complex interactions between numerous physical factors and their impact on flow fields. The ensuing can be employed to encapsulate the principal revelations garnered from this inquiry.

❖ Elevating the magnetic parameter M induces a lessening of fluid velocity across both Casson and Maxwell fluid instances, regardless of whether linear or nonlinear radiation is considered.
❖ Temperature profiles upsurge with growing values of Brownian motion, thermophoresis, and radiation parameters for both Casson and Maxwell fluids, in both linear and nonlinear radiation scenarios.
❖ Concentration profiles diminish as the chemical reaction parameter increases for both Casson and Maxwell fluids, across scenarios with and without activation energy. Conversely, concentration profiles heighten as activation energy values rise, encompassing both fluids and spanning both linear and nonlinear radiation cases.
❖ The influence of the magnetic field on the velocity distribution of the Maxwell fluid is more pronounced than its influence on the Casson fluid, particularly in scenarios involving nonlinear radiation.
❖ Within both fluid contexts, nonlinear thermal radiation has a more significant impact on enhancing the temperature profile and concentration distribution compared to linear thermal radiation.
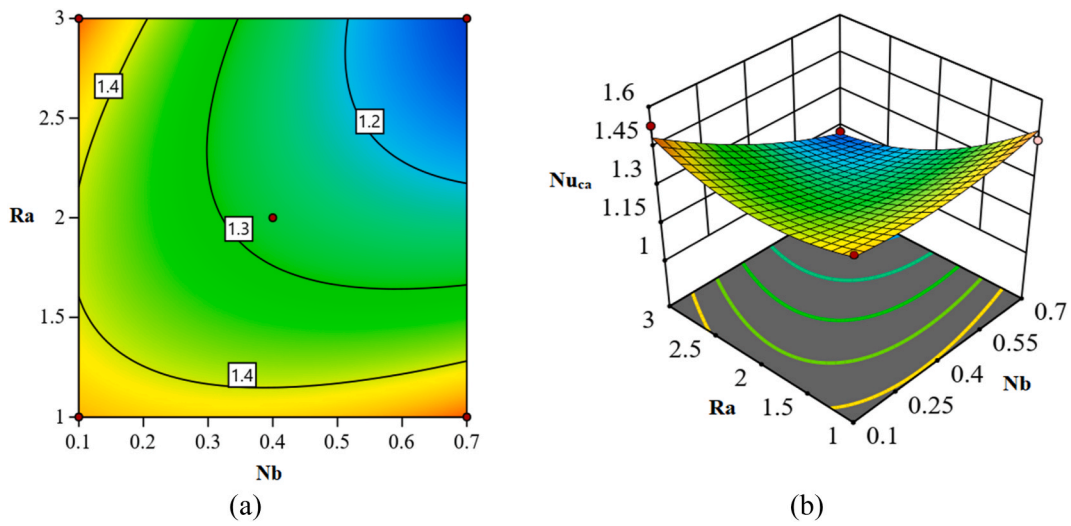
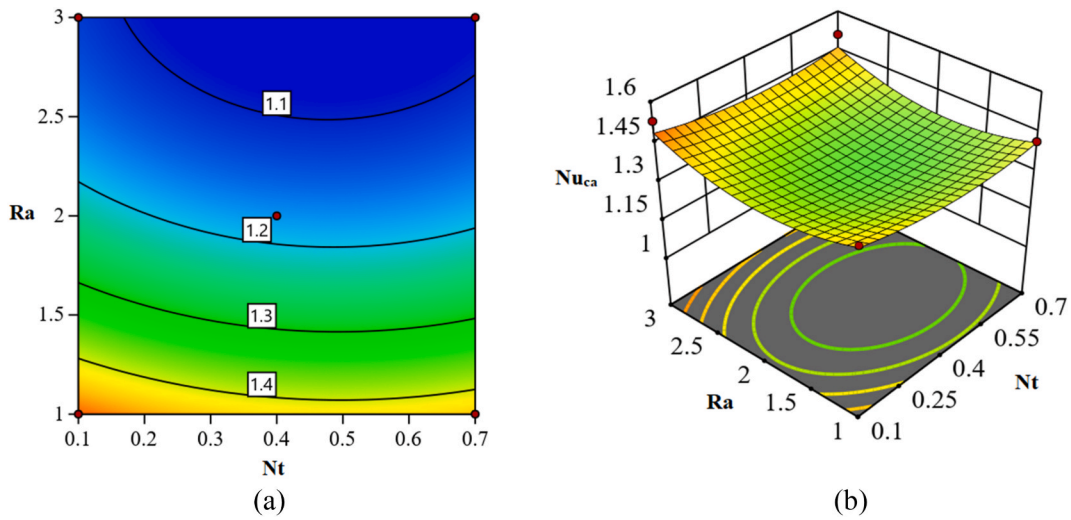**Fig. 29.** Effect of Nu_{ca} for Nb and Ra: (a) 2D and (b) 3D eyesight.

Fig. 30. Effect of Nu_{ca} for Nb and Ra: (a) 2D and (b) 3D eyesight.

Table 7
Sensitivity analysis for Nu_{max}.

Nb	Nt	Ra	$\dfrac{\partial Nu_{max}}{\partial Nb}$	$\dfrac{\partial Nu_{max}}{\partial Nt}$	$\dfrac{\partial Nu_{max}}{\partial Ra}$
−1	−1	0	−0.05	−0.0778	0.3275
	−1	1	−0.0461	−0.0696	0.4063
0	−1	0	−0.05	−0.0823	0.3314
	−1	1	−0.0461	−0.0741	0.4102
1	−1	0	−0.05	−0.0868	0.3353
	−1	1	−0.0461	−0.0786	0.4141

❖ The presence of activation energy exerts a more pronounced influence on enhancing the fluid's concentration profile in both Casson and Maxwell fluid cases.
❖ The sensitivity analysis demonstrations that the Ra parameter is positively sensitive on both Nu_{max} and Nu_{ca}, whereas Nt and Nb has negatively sensitive.
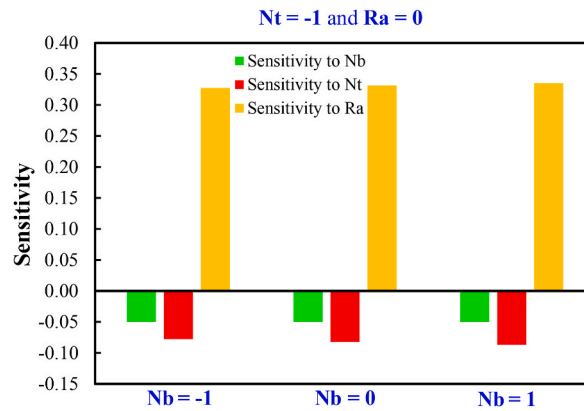
Fig. 31. Sensitivity of Nu_{max} at $Nb = -1$ and $Ra = 0$.

Table 8
Sensitivity analysis for Nu_{ca}.

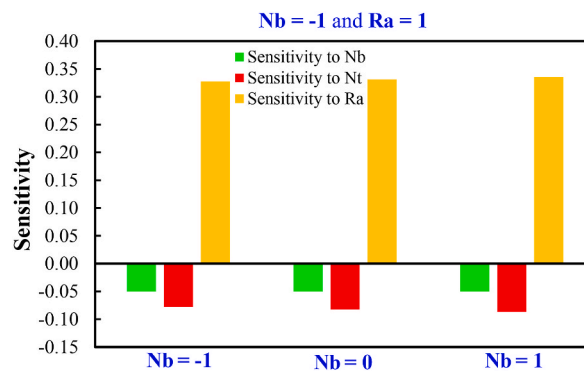| Nb	Nt	Ra	$\dfrac{\partial Nu_{ca}}{\partial Nb}$	$\dfrac{\partial Nu_{ca}}{\partial Nt}$	$\dfrac{\partial Nu_{ca}}{\partial Ra}$
−1	−1	0	−0.0718	−1.209	0.5797
	−1	1	−0.4083	−1.209	0.7263
0	−1	0	−0.0718	−1.209	0.2432
	−1	1	−0.4083	−1.209	0.3898
1	−1	0	−0.0718	−1.209	0.0933
	−1	1	−0.4083	−1.209	0.0533

Fig. 32. Sensitivity of Nu_{ca} at $Nb = -1$, and $Ra = 1$.

❖ Under the influence of nonlinear thermal radiation, the Casson fluid has influenced greatly than Maxwell fluid for the average heat transfer rate.

In the upcoming days, this examination could be extended to encompass various non-Newtonian fluids, such as fluids of higher grades like 3rd or 4th grade. This expansion would involve considering additional factors like exothermic/endothermic processes, microorganisms, exponential heat sources, and more. Additionally, enhanced numerical precision can be achieved by incorporating advanced techniques such as the Runge-Kutta based shooting method and implicit numerical schemes.

Limitations

In this study, the precision of the solution obtained through explicit FDM heavily relies on the spatial discretization, or the resolution of the grid. Consequently, striking a suitable equilibrium between accuracy and computational speed can present a formidable challenge. Moreover, the solution approach yields findings that are not any more accurate than those of some other methods (such as the Runge-Kutta and shooting methods). Furthermore, stability analysis and a convergence test are necessary to ensure the correctness of the answers produced by this approach, as it is not by default stable.

Data availability statement

The data that has been used is confidential.

CRediT authorship contribution statement

Saiful Islam: Writing – original draft, Validation, Software, Methodology, Investigation, Formal analysis, Conceptualization. **Md Yousuf Ali:** Writing – review & editing, Validation, Methodology, Investigation, Conceptualization. **Sk Reza-E-Rabbi:** Writing – review & editing, Supervision, Software, Methodology, Investigation.

Declaration of competing interest

The authors declare that they have no known competing financial interests or personal relationships that could have appeared to influence the work reported in this paper.

Nomenclature

$B_\circ$	magnetic field [$Wb.m^{-2}$]
C	liquid concentration [$mol.m^{-3}$]
Cf	skin friction coefficient [$-$]
cp	specific heat at constant pressure [$J.kg^{-1}.K^{-1}$]
Cw	fluid concentration at wall [$mol.m^{-3}$]
C_∞	fluid concentration outside the periphery [$mol.m^{-3}$]
E_y	yield stress [$N.m^{-2}$]
E_c	Eckert number [$-$]
EA	activation energy factor [$-$]
G_m	mass Grashof number [$-$]
G_r	Thermal Grashof number [$-$]
Kc	chemical reaction factor [$-$]
Le	Lewis number [$-$]
Kp	Porous term [$-$]
M	magnetic parameter [$-$]
Nb	Brownian motion factor [$-$]
Nt	thermophoresis factor [$-$]
Nu	Nusselt number [$-$]
Nu_{max}	Nusselt number for Maxwell fluid [$-$]
Nu_{ca}	Nusselt number for Casson fluid [$-$]
N_b	Brownian motion factor [$-$]
Nv	Maxwell parameter [$-$]
Pr	Prandtl number [$-$]
Ra	radiation parameter [$-$]
Sh	Sherwood number [$-$]
T	temperature [K]
Tw	temperature at surface [K]
$T\infty$	temperature outside the periphery [K]

Greek symbols

β_T	Coefficient of thermal expansion [K^{-1}]
β_C	concentration expansion exponent [K^{-1}]
β	Casson fluid parameter [$-$]
γ	temperature relative factor [$-$]
τ	Dimensionless time [$-$]
σ_s	Stefan-Boltzmann constant [$W.m^{-2}.K^{-4}$]
θ_w	temperature ratio [$-$]
θ	dimensionless temperature [$-$]
κ	thermal conductivity [$W.m^{-1}.K^{-1}$]
ε	Casson component [$-$]
ρ	Density of fluid [$kg.m^{-3}$]
ν	kinematic viscosity [$m^2.s^{-1}$]
φ	dimensionless concentration [$-$]

Abbreviation

2D   two dimensional
3D   three dimensional
EFD   explicit finite difference
RSM   response surface methodology

References

[1] S.U. Choi, J.A. Eastman, Enhancing Thermal Conductivity of Fluids with Nanoparticles, vol. 1, Argonne National Lab., IL (United States), 1995 (No. ANL/MSD/CP-84938; CONF-951135-29).

[2] O.A. Bég, M.S. Khan, I. Karim, M.M. Alam, M. Ferdows, Explicit numerical study of unsteady hydromagnetic mixed convective nanofluid flow from an exponentially stretching sheet in porous media, Appl. Nanosci. 4 (2014) 943–957.

[3] P. Biswas, S.M. Arifuzzaman, M. Rahman, M.S. Khan, Effects of periodic magnetic field on 2D transient optically dense gray nanofluid over a vertical plate: a computational EFDM study with SCA, Journal of Nanofluids 7 (2018) 82–91.

[4] T. Hayat, M.W. Ahmad, S.A. Khan, A. Alsaedi, Computational treatment of statistical declaration probable error for flow of nanomaterials with irreversibility, Adv. Mech. Eng. 14 (2022) 16878140211070937.

[5] J. Wang, Y.P. Xu, R. Qahiti, M. Jafaryar, M.A. Alazwari, N.H. Abu-Hamdeh, M.M. Selim, Simulation of hybrid nanofluid flow within a microchannel heat sink considering porous media analyzing CPU stability, J. Petrol. Sci. Eng. 208 (2022) 109734.

[6] A. Al-Mamun, S.M. Arifuzzaman, S. Reza-E-Rabbi, P. Biswas, M.S. Khan, Computational modelling on MHD radiative Sisko nanofluids flow through a nonlinearly stretching sheet, International Journal of Heat and Technology 37 (2019) 285–295.

[7] H.J. Xu, Z.B. Xing, F.Q. Wang, Z.M. Cheng, Review on heat conduction, heat convection, thermal radiation and phase change heat transfer of nanofluids in porous media: fundamentals and applications, Chem. Eng. Sci. 195 (2019) 462–483.

[8] A. Asadi, F. Pourfattah, I.M. Szilágyi, M. Afrand, G. Żyła, H.S. Ahn, O. Mahian, Effect of sonication characteristics on stability, thermophysical properties, and heat transfer of nanofluids: a comprehensive review, Ultrason. Sonochem. 58 (2019) 104701.

[9] M.S. Kamel, F. Lezsovits, Boiling heat transfer of nanofluids: a review of recent studies, Therm. Sci. 23 (2019) 109–124.

[10] T. Hayat, A. Aziz, A. Alsaedi, Analysis of entropy production and activation energy in hydromagnetic rotating flow of nanoliquid with velocity slip and convective conditions, J. Therm. Anal. Calorim. 146 (2021) 2561–2576.

[11] M.H. Esfe, H. Rostamian, D. Toghraie, M. Hekmatifar, A.T. Khalil Abad, Numerical study of heat transfer of U-shaped enclosure containing nanofluids in a porous medium using two-phase mixture method, Case Stud. Therm. Eng. 38 (2022) 102150.

[12] S. Islam, T. Bairagi, T. Islam, B.M.J. Rana, S. Reza-E-Rabbi, M.M. Rahman, Heatline visualization in hydromagnetic natural convection flow inside a prismatic heat exchanger using nanofluid, International Journal of Thermofluids 16 (2022) 100248.

[13] T. Hayat, M.W. Ahmad, S.A. Khan, A. Alsaedi, Computational treatment of statistical declaration probable error for flow of nanomaterials with irreversibility, Adv. Mech. Eng. 14 (2022) 1–13.

[14] E.A. Sayed, M. Fathy, Numerical study of flow and heat transfer of a nanofluid past a vertical cone, Case Stud. Therm. Eng. 34 (2022) 102038.

[15] T. Hageman, R. de Borst, Flow of non-Newtonian fluids in fractured porous media: isogeometric vs standard finite element discretization, Int. J. Numer. Anal. Methods GeoMech. 43 (2019) 2020–2037.

[16] H. Waqas, M. Imran, M.M. Bhatti, Bioconvection aspects in non-Newtonian three-dimensional Carreau nanofluid flow with Cattaneo-Christov model and activation energy, The European Physical Journal Special Topics 230 (2021) 1317–1330.

[17] S. Hosseinzadeh, K. Hosseinzadeh, A. Hasibi, D.D. Ganji, Hydrothermal analysis on non-Newtonian nanofluid flow of blood through porous vessels, Proc. IME E J. Process Mech. Eng. 236 (2022) 1604–1615.

[18] J. Mustafa, S. Alqaed, M. Sharifpur, Numerical study on performance of double-fluid parabolic trough solar collector occupied with hybrid non-Newtonian nanofluids: investigation of effects of helical absorber tube using deep learning, Eng. Anal. Bound. Elem. 140 (2022) 562–580.

[19] L. Ali, B. Ali, X. Liu, T. Iqbal, R.M. Zulqarnain, M. Javid, A comparative study of unsteady MHD Falkner–Skan wedge flow for non-Newtonian nanofluids considering thermal radiation and activation energy, Chin. J. Phys. 77 (2022) 1625–1638.

[20] M.K. Raihan, P.P. Jagdale, S. Wu, X. Shao, J.B. Bostwick, X. Pan, X. Xuan, Flow of non-Newtonian fluids in a single-cavity microchannel, Micromachines 12 (2021) 836.

[21] J.C. Maxwell, On the dynamical theory of gases, Philosophical transactions of the Royal Society of London. 157 (1867) 49–88.

[22] M.S. Abel, J.V. Tawade, M.M. Nandeppanavar, MHD flow and heat transfer for the upper-convected Maxwell fluid over a stretching sheet, Meccanica 47 (2012) 385–393.

[23] T. Hayat, Z. Bashir, S. Qayyum, A. Alsaedi, Investigation of double diffusion Cattaneo-Christov model in mixed convection flow by variable thickness surface, Results in physics 7 (2017) 3873–3881.

[24] S.M. Arifuzzaman, M.S. Khan, M.S. Islam, M.M. Islam, B.M.J. Rana, P. Biswas, S.F. Ahmmed, *MHD Maxwell fluid flow in presence of nano-particle through a vertical porous–plate with heat-generation, radiation absorption and chemical reaction*, Heat Mass Tran. 9 (2017) 1–14.

[25] S. Ahmad, H.H. Coban, M.N. Khan, U. Khan, Q.H. Shi, T. Muhammad, R. Chinram, S. Kadry, Computational analysis of the unsteady 3D chemically reacting MHD flow with the properties of temperature dependent transpose suspended Maxwell nanofluid, Case Stud. Therm. Eng. 26 (2021) 101169.

[26] R. Safdar, M. Jawad, S. Hussain, M. Imran, A. Akgül, W. Jamshed, Thermal radiative mixed convection flow of MHD Maxwell nanofluid: implementation of buongiorno's model, Chin. J. Phys. 77 (2022) 1465–1478.

[27] N. Casson, A flow equation for pigment-oil suspensions of the printing ink type, Rheol. Disperse Syst. (1959) 84–104.

[28] A. Al-Mamun, S.M. Arifuzzaman, U.S. Alam, S. Islam, M. Khan, Numerical simulation of periodic MHD Casson nanofluid flow through porous stretching sheet, SN Appl. Sci. 3 (2021) 1–14.

[29] S.B. Chen, N. Shahmir, M. Ramzan, Y.L. Sun, A.A. Aly, M.Y. Malik, Thermophoretic particle deposition in the flow of dual stratified Casson fluid with magnetic dipole and generalized Fourier's and Fick's laws, Case Stud. Therm. Eng. 26 (2021) 101186.

[30] S. Bilal, K.K. Asogwa, H. Alotaibi, M.Y. Malik, I. Khan, Analytical treatment of radiative Casson fluid over an isothermal inclined Riga surface with aspects of chemically reactive species, Alex. Eng. J. 60 (2021) 4243–4253.

[31] M.R. Khan, A.S. Al-Johani, A.M. Elsiddieg, T. Saeed, A.M. AbdAllah, The computational study of heat transfer and friction drag in an unsteady MHD radiated Casson fluid flow across a stretching/shrinking surface, Int. Commun. Heat Mass Tran. 130 (2022) 105832.

[32] I.A. Shah, S. Bilal, S. Noeiaghdam, U. Fernandez-Gamiz, H. Shahzad, Thermosolutal natural convection energy transfer in magnetically influenced Casson fluid flow in hexagonal enclosure with fillets, Results in Engineering 15 (2022) 100584.

[33] P. Das, Sarifuddin, J. Rana, P.K. Mandal, Solute dispersion in transient Casson fluid flow through stenotic tube with exchange between phases, Phys. Fluids 33 (2021) 061907.

[34] U. Khan, F. Mebarek-Oudina, A. Zaib, A. Ishak, S. Abu Bakar, E.S.M. Sherif, D. Baleanu, An exact solution of a Casson fluid flow induced by dust particles with hybrid nanofluid over a stretching sheet subject to Lorentz forces, Waves Random Complex Media (2022) 1–14.

[35] A. Dawar, Z. Shah, H.M. Alshehri, S. Islam, P. Kumam, Magnetized and non-magnetized Casson fluid flow with gyrotactic microorganisms over a stratified stretching cylinder, Sci. Rep. 11 (2021) 1–14.

[36] C. Sulochana, G.P. Ashwinkumar, N. Sandeep, Similarity solution of 3D Casson nanofluid flow over a stretching sheet with convective boundary conditions, Journal of the Nigerian Mathematical Society 35 (2016) 128–141.

[37] T. Thumma, A. Wakif, I.L. Animasaun, Generalized differential quadrature analysis of unsteady three-dimensional MHD radiating dissipative Casson fluid conveying tiny particles, Heat Transfer 49 (2020) 2595–2626.

[38] F. Ali, N.S. Ahmad, I. Khan, M. Saqib, Magnetic field effect on blood flow of Casson fluid in axisymmetric cylindrical tube: a fractional model, J. Magn. Magn. Mater. 423 (2017) 327–336.

[39] S. Priyadharshini, R. Ponalagusamy, Mathematical modelling for pulsatile flow of Casson fluid along with magnetic nanoparticles in a stenosed artery under external magnetic field and body acceleration, Neural Comput. Appl. 31 (2019) 813–826.

[40] A. Ali, H. Farooq, Z. Abbas, Z. Bukhari, A. Fatima, Impact of Lorentz force on the pulsatile flow of a non-Newtonian Casson fluid in a constricted channel using Darcy's law: a numerical study, Sci. Rep. 10 (2020) 1–15.

[41] Z. Bukhari, A. Ali, Z. Abbas, H. Farooq, The pulsatile flow of thermally developed non-Newtonian Casson fluid in a channel with constricted walls, AIP Adv. 11 (2021) 025324.

[42] M. Awais, M.A.Z. Raja, S.E. Awan, M. Shoaib, H.M. Ali, Heat and mass transfer phenomenon for the dynamics of Casson fluid through porous medium over shrinking wall subject to Lorentz force and heat source/sink, Alex. Eng. J. 60 (2021) 1355–1363.

[43] M. Tencer, J.S. Moss, T. Zapach, Arrhenius average temperature: the effective temperature for non-fatigue wearout and long term reliability in variable thermal conditions and climates, IEEE Trans. Compon. Packag. Technol. 27 (2004) 602–607.

[44] A.R. Bestman, Radiative heat transfer to flow of a combustible mixture in a vertical pipe, Int. J. Energy Res. 15 (1991) 179–184.

[45] M. Khan, T. Salahuddin, M.Y. Malik, F. Khan, Arrhenius activation in MHD radiative Maxwell nanoliquid flow along with transformed internal energy, The European Physical Journal Plus 134 (2019) 198.

[46] R. Kalaivanan, N.V. Ganesh, Q.M. Al-Mdallal, An investigation on Arrhenius activation energy of second grade nanofluid flow with active and passive control of nanomaterials, Case Stud. Therm. Eng. 22 (2020) 100774.

[47] A. Saeed, T. Gul, Bioconvection Casson nanofluid flow together with Darcy-Forchheimer due to a rotating disk with thermal radiation and Arrhenius activation energy, SN Appl. Sci. 3 (2021) 1–19.

[48] Q.H. Shi, A. Hamid, M.I. Khan, R.N. Kumar, R.J. Gowda, B.C. Prasannakumara, J.D. Chung, Numerical study of bio-convection flow of magneto-cross nanofluid containing gyrotactic microorganisms with activation energy, Sci. Rep. 11 (2021) 1–15.

[49] F. Ahmed, S. Reza-E-Rabbi, M.Y. Ali, L.E. Ali, A. Islam, M.A. Rahman, R. Roy, M.R. Islam, S.F. Ahmmed, Numerical modeling of a MHD non-linear radiative Maxwell nano fluid with activation energy, Heliyon 10 (2024) e24098.

[50] M.Y. Ali, S. Reza-E-Rabbi, S.F. Ahmmed, M.N. Nabi, A.K. Azad, S.M. Muyeen, Hydromagnetic flow of Casson nano-fluid across a stretched sheet in the presence of thermoelectric and radiation, International Journal of Thermofluids 21 (2024) 100484.

[51] G.B. Dharmaiah, S. Goud, N.A. Shah, M. Faisal, Numerical analysis of heat and mass transfer with viscous dissipation, Joule dissipation, and activation energy, Int. J. Ambient Energy 44 (2023) 2090–2102.

[52] G. Dharmaiah, F. Mebarek-Oudina, M.S. Kumar, K.C. Kala, Nuclear reactor application on Jeffrey fluid flow with Falkner-skan factor, Brownian and thermophoresis, non linear thermal radiation impacts past a wedge, J. Indian Chem. Soc. 100 (2023) 100907.

[53] G. Dharmaiah, J.L.R. Prasad, K.S. Balamurugan, I. Nurhidayat, U. Fernandez-Gamiz, S. Noeiaghdam, Performance of magnetic dipole contribution on ferromagnetic non-Newtonian radiative MHD blood flow: an application of biotechnology and medical sciences, Heliyon 9 (2023) e13369.

[54] T.P. Kumar, G. Dharmaiah, K. AL-Farhany, A. Abdulkadhim, M.A. Alomari, M.H. Abdulsada, W. Jamshed, M.R. Eid, H. Alqahtani, Transient conditions effects on electromagnetic Casson fluid flow via stretching surface: system thermal case elaboration, Numer. Heat Tran., Part B: Fundamentals (2023) 1–17.

[55] S. Goud, G. Dharmaiah, Role of Joule heating and activation energy on MHD heat and mass transfer flow in the presence of thermal radiation, Numer. Heat Tran., Part B: Fundamentals. (2023) 1–122.

[56] S. Reza-E-Rabbi, S.F. Ahmmed, S.M. Arifuzzaman, T. Sarkar, M.S. Khan, Computational modelling of multiphase fluid flow behaviour over a stretching sheet in the presence of nanoparticles, Engineering Science and Technology, an International Journal 23 (2020) 605–617.

[57] B. Carnahan, H.A. Luther, J.O. Wilkes, Applied Numerical Methods, John Wiley and Sons, New York, 1969.

[58] S. Reza-E-Rabbi, S.F. Ahmmed, S. Islam, S.M. Arifuzzaman, B.M.J. Rana, M.Y. Ali, A. Al-Mamun, M.S. Khan, Characterization of fluid flow and heat transfer of a periodic magnetohydrodynamics nano non-Newtonian liquid with Arrhenius activation energy and nonlinear radiation, Heat Transfer 51 (2022) 6578–6615.

[59] M.Y. Ali, S. Reza-E-Rabbi, M.M.H. Rasel, S.F. Ahmmed, *Combined impacts of thermoelectric and radiation on hydromagnetic nanofluid flow over a nonlinear stretching sheet*, Partial Differential Equations, Appl. Math. 7 (2023) 100500.

[60] M.R. Islam, S. Reza-E-Rabbi, M.Y. Ali, M.M.H. Rasel, S.F. Ahmmed, Numerical simulation of mass and heat transport phenomena of hydromagnetic flow of Casson fluid with sinusoidal boundary conditions, Engineering Reports (2022) 12659.

[61] D.C. Montgomery, Design and Analysis of Experiments, John Wiley & sons., 2017.

[62] G.E. Box, K.B. Wilson, On the experimental attainment of optimum conditions, Breakthroughs in statistics: methodology and distribution (1992) 270–310.

[63] F. Campolongo, R. Braddock, The use of graph theory in the sensitivity analysis of the model output: a second order screening method, Reliab. Eng. Syst. Saf. 64 (1999) 1–12.